

Magnetically regulated collapse in the B335 protostar?

II. Observational constraints on gas ionization and magnetic field coupling

Victoria Cabedo^{1,3}, Anaëlle Maury^{1,2}, Josep Miquel Girart^{3,4}, Marco Padovani⁵, Patrick Hennebelle¹, Martin Houde⁶ and Qizhou Zhang²

¹ Astrophysics department, CEA/DRF/IRFU/DAp, Université Paris Saclay, UMR AIM, F-91191 Gif-sur-Yvette, France
e-mail: vcabedo.93@gmail.com

² Center for Astrophysics | Harvard & Smithsonian, 60 Garden Street, Cambridge, MA 02138, USA

³ Institut de Ciències de l'Espai (ICE), CSIC, Can Magrans s/n, E-08193 Cerdanyola del Vallès, Catalonia, Spain

⁴ Institut d'Estudis Espacials de Catalunya (IEEC), E-08034 Barcelona, Catalonia, Spain

⁵ INAF–Osservatorio Astrofisico di Arcetri, Largo E. Fermi 5, 50125 Firenze, Italy

⁶ Department of Physics and Astronomy, The University of Western Ontario, 1151 Richmond Street, London, Ontario N6A 3K7, Canada

Preprint online version: April 22, 2022

ABSTRACT

Context. It is still largely debated whether magnetic fields play a key role in dynamically shaping the products of the star formation process. For example, in magnetized protostellar formation models, magnetic braking plays a major role in the regulation of the angular momentum transported from large envelope scales to the inner envelope, and is expected to be responsible for the resulting protostellar disk sizes. However, non-ideal magnetohydrodynamic effects that rule the coupling of the magnetic field to the gas also depend heavily on the local physical conditions, such as the ionization fraction of the gas.

Aims. The purpose of this work is to observationally characterize the level of ionization of the gas at small envelope radii and investigate its relation to the efficiency of the coupling between the star-forming gas and the magnetic field in the Class 0 protostar B335.

Methods. We have obtained molecular line emission maps of B335 with ALMA, which we use to measure the deuteration fraction of the gas, R_D , its ionization fraction, χ_e , and the cosmic-ray ionization rate, ζ , at envelope radii $\lesssim 1000$ au.

Results. We find large fractions of ionized gas, $\chi_e \simeq 1 - 8 \times 10^{-6}$. Our observations also reveal an enhanced ionization that increases at small envelope radii, reaching values up to $\zeta \simeq 10^{-14} \text{ s}^{-1}$ at a few hundred au from the central protostellar object. We show that this extreme ionization rate can be attributed to the presence of cosmic rays accelerated close to the protostar.

Conclusions. We report the first resolved map of the cosmic-ray ionization rate at scales $\lesssim 1000$ au in a solar-type Class 0 protostar, finding remarkably high values. Our observations suggest that local acceleration of cosmic rays, and not the penetration of interstellar Galactic cosmic rays, may be responsible for the gas ionization in the inner envelope, potentially down to disk forming scales. If confirmed, our findings imply that protostellar disk properties may also be determined by local processes setting the coupling between the gas and the magnetic field, and not only by the amount of angular momentum available at large envelope scales and the magnetic field strength in protostellar cores. We stress that the gas ionization we find in B335 significantly stands out from the typical values routinely used in state-of-the-art models of protostellar formation and evolution. If the local processes of ionization uncovered in B335 are prototypical to low-mass protostars, our results are calling for revising the treatment of ionizing processes in magnetized models for star and disk formation.

Key words. Stars: formation, circumstellar matter – ISM: magnetic fields, chemistry – Techniques: interferometry

1. Introduction

Observational studies have shown that magnetic fields are present at all scales where star formation processes are at work, permeating molecular clouds, prestellar cores and protostellar envelopes (e.g., Girart et al. 2006; Alves et al. 2014; Zhang et al. 2014; Soler 2019). While magnetized models of star formation have been developed early on, it is only recently that complex physics is included in numerical magnetohydrodynamic (MHD) models, and that the predictions of dedicated models are directly compared to observations of star-forming regions. One of the major achievements of magnetized models is the prediction of small sizes for protostellar disks, regulated by magnetic braking (Dapp et al. 2012; Hennebelle & Inutsuka 2019; Zhao

et al. 2020). Recent observations have indeed shown that disks are compact, almost an order of magnitude smaller than those produced in purely hydrodynamical models (Maury et al. 2019; Lebreuilly et al. 2021).

In magnetized collapse models, non-ideal MHD effects play a major role in the regulation of the magnetic flux during the early stages of protostellar formation (Machida et al. 2011; Li et al. 2011; Marchand et al. 2020). Hence, these processes indirectly limit the angular momentum transported by the magnetic field from large envelope scales to the inner envelope, and set the resulting disk size. However, these resistive processes depend heavily on the local physical conditions, such as dust grain properties (electric charge and size), gas density and temperature, density of ions and electrons, and the cosmic-ray (CR) ion-

ionization rate, ζ (namely the number of molecular hydrogen ionization per unit time, see e.g., Zhao et al. 2020, for a review). Observationally, only very few measurements of these quantities have been obtained toward solar-type protostars: the effective coupling of magnetic fields to the infalling-rotating material, at scales where the circumstellar material feeds the growth in mass of the protostellar embryo and its disk, is thus still largely unknown.

B335, located at a distance of 164.5 pc (Watson 2020), is an isolated Bok Globule which contains an embedded Class 0 protostar (Keene et al. 1983). The core is associated with an east-west outflow that is prominently detected in CO, with an inclination of 10° on the plane of the sky and an opening angle of 45° (Hirano et al. 1988, 1992; Stutz et al. 2008; Yen et al. 2010). Its isolation and relative proximity has made of B335 an ideal object to test models of star formation. Asymmetric double-peaked line profiles observed in the molecular emission of the gas toward the envelope have been interpreted as optically thick lines tracing infalling motions, and have been extensively used to derive mass infall rates from 10^{-7} to $\sim 3 \times 10^{-6} M_\odot \text{ yr}^{-1}$ at radii of 100–2000 au (Zhou et al. 1993; Yen et al. 2010; Evans et al. 2015). However, new observations of optically thin emission from less abundant molecules revealed the presence of two velocity components tracing non-symmetric motions at these envelope scales, which could contribute significantly to the double-peaked line profiles (Cabedo et al. 2021). These results have suggested that simple spherically symmetric infall models might not be adequate to describe the collapse of the B335 envelope, and tentatively unveiled the existence of preferential accretion streamlines along outflow cavity walls.

B335 is also an excellent prototype for the study of magnetized star formation models, since it has been proposed as an example of protostar where the disk size is set by a magnetically regulated collapse (Maury et al. 2018, hereafter Paper I). This hypothesis surges mainly from two observations. First, the rotation of the gas observed at large envelope radii is not found at small envelope radii (< 1000 au) and no kinematic signature of a disk was reported down to ~ 10 au (Kurono et al. 2013; Yen et al. 2015). Second, observations of polarized dust emission have revealed an "hourglass" magnetic field morphology (Paper I) in the inner envelope: their comparisons to MHD models of protostellar formation (see e.g., Masson et al. 2016; Hennebelle et al. 2020, for a whole description of the models) suggest that the B335 envelope is threaded by a rather strong magnetic field which is well coupled to the infalling-rotating gas, preventing the disk growth to large radii. The purpose of the analysis presented here is to characterize the level of ionization and its origin in order to test the model scenario proposed in Paper I, and put observational constraints on the efficiency of the coupling of the magnetic field to the star-forming gas in the inner envelope of B335.

In Sec. 2 we present the ALMA observations used to constrain physical and chemical properties of the gas at envelope radii $\lesssim 1000$ au. In Sec. 3 we derive the deuteration fraction from DCO^+ ($J=3-2$) and H^{13}CO^+ ($J=3-2$). In Sec. 4 we compute the ionization fraction and the CR ionization rate. Finally, in Sec. 5, we discuss our results concerning deuteration processes, the ionization, the possible influence of a local source of radiation and its effect on the coupling between the gas and the magnetic field.

2. Observations and data reduction

Observations of the Class 0 protostellar object B335 were carried out with the ALMA interferometer during the Cycle 4 observation period, from October 2016 to September 2017, as part of the 2016.1.01552.S project. The centroid position of B335 is assumed to be $\alpha = 19:37:00.9$ and $\delta = +07:34:09.6$ (in J2000 coordinates), as the dust continuum peak obtained by Maury et al. (2018).

We used DCO^+ ($J=3-2$) and H^{13}CO^+ ($J=3-2$) to obtain the deuteration fraction and the ionization fraction. We used H^{13}CO^+ ($J=1-0$) and C^{17}O ($J=1-0$) to derive the hydrogenation fraction. Additionally, we observed the dust continuum at 110 GHz to derive the estimated line opacities, CO depletion factor and ionization rate. We also targeted ^{12}CO ($J=2-1$) and N_2D^+ ($J=3-2$) for comparison purposes. All lines were targeted using a combination of ALMA configurations to recover the largest lengthscale range possible. Since our data for H^{13}CO^+ ($J=3-2$) only included observations with the Atacama Compact Array (ACA), we used additional observations of this molecular line at smaller scales from the ALMA project 2015.1.01188.S. Technical details of the ALMA observations are shown in Appendix A.

Calibration of the raw data was done using the standard script for Cycle 4 ALMA data using the Common Astronomy Software Applications (CASA), version 5.6.1-8. The continuum emission was self-calibrated with CASA. Line emission from ^{12}CO ($J=2-1$) and N_2D^+ ($J=3-2$) was additionally calibrated using the self-calibrated continuum model at the appropriate frequency (231 GHz, not shown in this work).

Final images of the data were generated from the calibrated visibilities using the tCLEAN algorithm within CASA, using Briggs weighting with a robust parameter of 1 for all the tracers. Since we want to compare our data to the C^{17}O ($J=1-0$) emission presented in Cabedo et al. (2021), we adjust our imaging parameters to obtain matching beam maps with similar angular and spectral resolution. For DCO^+ ($J=3-2$) and H^{13}CO^+ ($J=3-2$) we restricted the baselines to a common u, v -range, between 9 and $140 k\lambda$, and finally smoothed them to the same angular resolution. The preliminary analysis shows that both, C^{17}O ($J=1-0$) and H^{13}CO^+ ($J=1-0$), emission is barely detected in the most extended configurations. We proceed by applying a common *uv-tapering* of $1.5''$ to both lines. This procedure allows weighting down the largest baselines, giving more weight to the smaller baselines and allowing to obtain a better S/N. Furthermore, we smoothed the data to obtain exactly the same angular resolution. Additionally, we smooth C^{17}O ($J=1-0$) and the dust continuum at 110 GHz to obtain DCO^+ matching beam maps to compute the depletion factor. The imaging parameters used to obtain all the spectral cubes and their final characteristics are shown in Table 1. Even though the characteristics and properties of the C^{17}O ($J=1-0$) maps are slightly different than the ones presented in Cabedo et al. (2021), due to the differences in the imaging process, the line profiles show the same characteristics, i.e., line profiles are double-peaked and present the same velocity pattern at different offsets from the center of the source, confirming that the imaging process has no large effect on the shape of the line profile, and that the two velocity components can still be observed.

2.1. Data products

From the data cubes, we obtained spectral maps that present the spectrum (in velocity units) at each pixel of a determined region

Table 1: Imaging parameters and final maps characteristics.

	DCO ⁺ (J=3-2)	H ¹³ CO ⁺ (J=3-2)	¹² CO (J=2-1)	N ₂ D ⁺ (J=3-2)	H ¹³ CO ⁺ (J=1-0)	C ¹⁷ O** (J=1-0)	cont.
Rest. Freq. (GHz)	216.112	260.255	230.538	231.321	86.754	112.359	110
Θ_{LRS}^* (arcsec)	11.3	16.0	10.6	10.6			22.3
Pixel size (arcsec)	0.5	0.5	0.5	0.5	0.25	0.25	0.3
Θ_{maj} (arcsec)	1.5	1.5	1.5	1.5	2.6	2.6	0.8
Θ_{min} (arcsec)	1.5	1.5	1.5	1.5	2.6	2.6	0.7
P.A. (°)	0	0	0	0	0	0	-61.5
Spectral res. (km s ⁻¹)	0.2	0.2	0.2	0.2	0.15	0.15	-
rms (mJy beam ⁻¹)	22.37	53.15	143.5	6.00	18.58	10.57	0.065
vel. range (km s ⁻¹)	7.8 - 8.9	7.5 - 8.9	7.6 - 9.4	7.7 - 8.9	7.4-9.2	4.7-6.5 7.7-9.3	-
rms (mJy beam ⁻¹ km s ⁻¹)	11.17	21.28	634.6	5.23	17.17	17.58	-

* Largest recoverable scale, computed as $\Theta_{\text{LRS}} = 206265(0.6\lambda/b_{\text{min}})$ in arcsec, where λ is the rest wavelength of the line, and b_{min} is the minimum baseline of the configuration, both in m (Asayama et al. 2016).

** The two velocity ranges correspond to the two resolved hyperfine components.

around the center of the source. These maps allow to evaluate the spectra at different offsets from the center of the envelope where the dust continuum emission peak localizes the protostar, and to detect any distinct line profile or velocity pattern. The obtained spectral maps are discussed in Appendix B.1.

We derived the integrated intensity maps by integrating the molecular line emission over the velocity range in which it is emitting (the velocity range used for each molecule is shown in Table 1). Figure 1 shows the dust continuum emission map at 110 GHz and the integrated intensity contours of C¹⁷O (J=1-0), DCO⁺ (J=3-2), H¹³CO⁺ (J=1-0) and H¹³CO⁺ (J=3-2). The H¹³CO⁺ (J=1-0) emission clearly appears more spatially extended than the other lines, roughly following most of the dust emission. The emission from this line extends further than the dust toward the south-east outflow cavity wall direction. The C¹⁷O (J=1-0), DCO⁺ (J=3-2) and H¹³CO⁺ (J=3-2) emission present a similar, relatively compact, morphology centered around the dust peak and elongated along the north-south equatorial plane. However, the spatial extent along the equatorial plane is slightly more compact for the H¹³CO⁺ emission (~2100 au) than the DCO⁺ emission (~2500 au), and both are more extended than C¹⁷O (~1700 au). The DCO⁺ peak intensity is clearly more displaced from the continuum peak than the H¹³CO⁺ (J=3-2) peak, this could be a local effect around the protostar due to the large temperature and irradiation conditions, which destroy DCO⁺. The C¹⁷O (J=1-0) emission appears to be slightly extended along the outflow cavities.

Since all the molecules present a double-peaked profile with similar velocity patterns as the ones observed in Cabedo et al. (2021), namely two different velocity components with varying intensity across the source spatial extent, we use two independent velocity components to fit simultaneously the line profiles. Following Cabedo et al. (2021), we modeled the spectrum at each pixel by using the *HfS* fitting program (Estalella 2017). We obtained maps of peak velocity and velocity dispersion for each velocity component, deriving the corresponding uncertainties from the χ^2 goodness of fit (see Estalella 2017, for a thorough description of the derivation of uncertainties). A more detailed discussion of these maps is presented in Appendix B.2. In addition, an estimate of line opacities is given in Appendix C. In the following sections, the statistical uncertainties derived for deuteration fraction, ionization fraction, and ionization rate

(shown in Figs. 2, 4, and 5, respectively) are computed using standard error propagation analysis from the uncertainties of each parameter obtained with the line modeling (peak velocity, velocity dispersion, and opacity). Other systematic uncertainties are discussed separately in the corresponding sections.

3. Deuteration fraction

The process of deuteration consists of an enrichment of the amount of deuterium with respect to hydrogen in molecular species. The deuteration fraction, $R_D = [D]/[H]$, in molecular ions, in particular HCO⁺, has been extensively used as an estimator of the degree of ionization in molecular gas (Caselli et al. 1998; Fontani et al. 2017). We apply here this method to obtain maps of R_D , computed as the column density ratio of DCO⁺ (J=3-2) and its non-deuterated counterpart, H¹³CO⁺ (J=3-2):

$$R_D = \frac{1}{f_{12/13}C} \frac{N_{\text{DCO}^+}}{N_{\text{H}^{13}\text{CO}^+}}, \quad (1)$$

where N_i is the column density of each species and $f_{12/13}C$ is the abundance ratio of ¹²C to ¹³C. The column density of both species is computed such as:

$$N_i = \frac{8\pi}{\lambda^3 A} \frac{1}{J_v(T_{\text{ex}}) - J_v(T_{\text{bg}})} \times \frac{1}{1 - \exp(-hv/k_B T_{\text{ex}})} \frac{Q_{\text{rot}}}{g_u \exp(-E_l/k_B T_{\text{ex}})} \times \int I_0 dv, \quad (2)$$

where λ is the wavelength of the transition, A is the Einstein coefficient, $J_v(T)$ is the Planck function at the background (2.7 K) and at the excitation temperature of the line (assumed to be 25 K), k_B is the Boltzmann constant, g_u is the upper state degeneracy, Q_{rot} is the partition function at 25 K, E_l is the energy of the lower level, and $\int I_0 dv$ is the integrated intensity. Values of these parameters for each molecule are listed in Table 2.

The top panels of Fig. 2 show the R_D maps of B335 for the blue- and red-shifted velocity components (left and right column, respectively). The mean values of the deuteration fraction

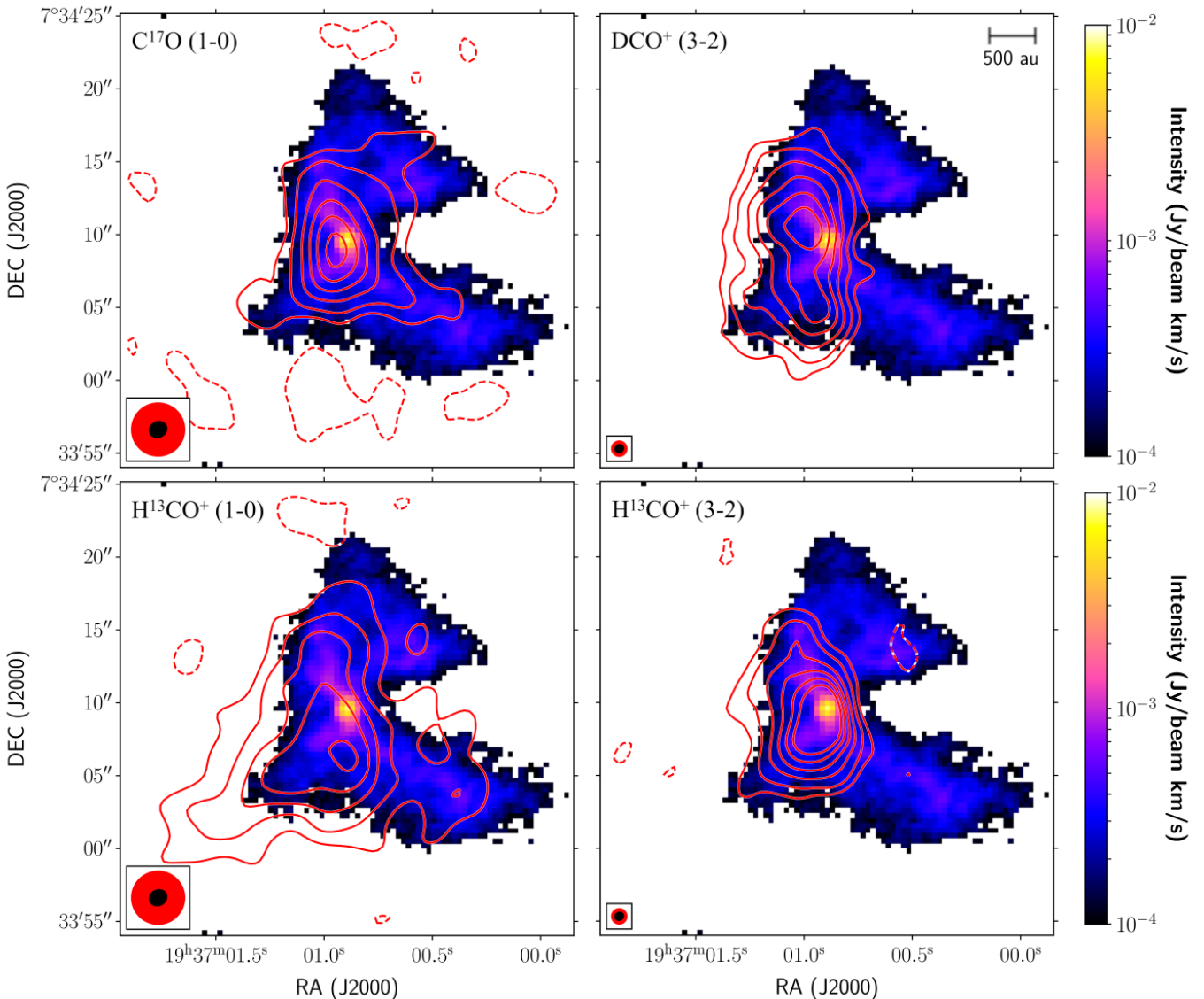


Fig. 1: Map of the dust continuum emission at 110 GHz clipped for values smaller than 3σ (see Table 1) and integrated emission for the four molecular lines as indicated in the upper left corner (red contours). Contours are $-2, 3, 5, 8, 11, 14$ and 17σ (the individual σ values are indicated in Table 1). The velocity ranges used to obtain the integrated intensity maps are shown in Table 1. In the bottom-left of each plot is shown the beam size for each molecular line (in red) and for the dust continuum emission (in black). The physical scale is shown in the top-right corner of the figure.

Table 2: Parameters for the computation of the column density.

Transition	DCO ⁺ (J=3-2)	H ¹³ CO ⁺ (J=3-2)	C ¹⁷ O (J=1-0)
$\log (A/s^{-1})$	-3.12	-2.87	-7.17
g_u	7	7	3
Q_{rot}	25.22	22.91	25
E_l (cm ⁻¹)	7.21	8.68	0.00
N_i^{mean} (cm ⁻²)	3×10^{11}	7×10^{11}	3×10^{13}

are $\sim 1\text{-}2\%$, being higher in the outer region of the envelope, where the gas is expected to be colder, and decreasing toward the center, where the protostar is located and the temperature is expected to rise. The bottom panels show that the statistical uncertainties are roughly one tenth of the deuteration values. We note that the highest values of R_D are found for the blue-shifted com-

ponent, as high as 3.5%. However, these values have the largest associated errors due to the presence of a third velocity component in the line profiles of H¹³CO⁺ (J=3-2) and should not be totally trusted (see Appendix B.1). Finally, we note that while the average R_D values for both velocity components are similar, the most widespread blue-shifted gas component shows larger R_D dispersion, with values from 0.06 to 2%, while the more localized red-shifted gas exhibits more uniform values, between 0.01 and 1%.

One of the main uncertainties of the deuteration analysis is the assumption that both DCO⁺ (J=3-2) and H¹³CO⁺ (J=3-2) have the same T_{ex} . This should be accurate enough, since both molecules present a similar geometry and dipolar moment and are assumed to be spatially coexistent. However, to check the effect that the variation of T_{ex} would produce in our values, we computed the column densities of both species at two additional temperatures, 20 and 30 K. While the DCO⁺ column density do

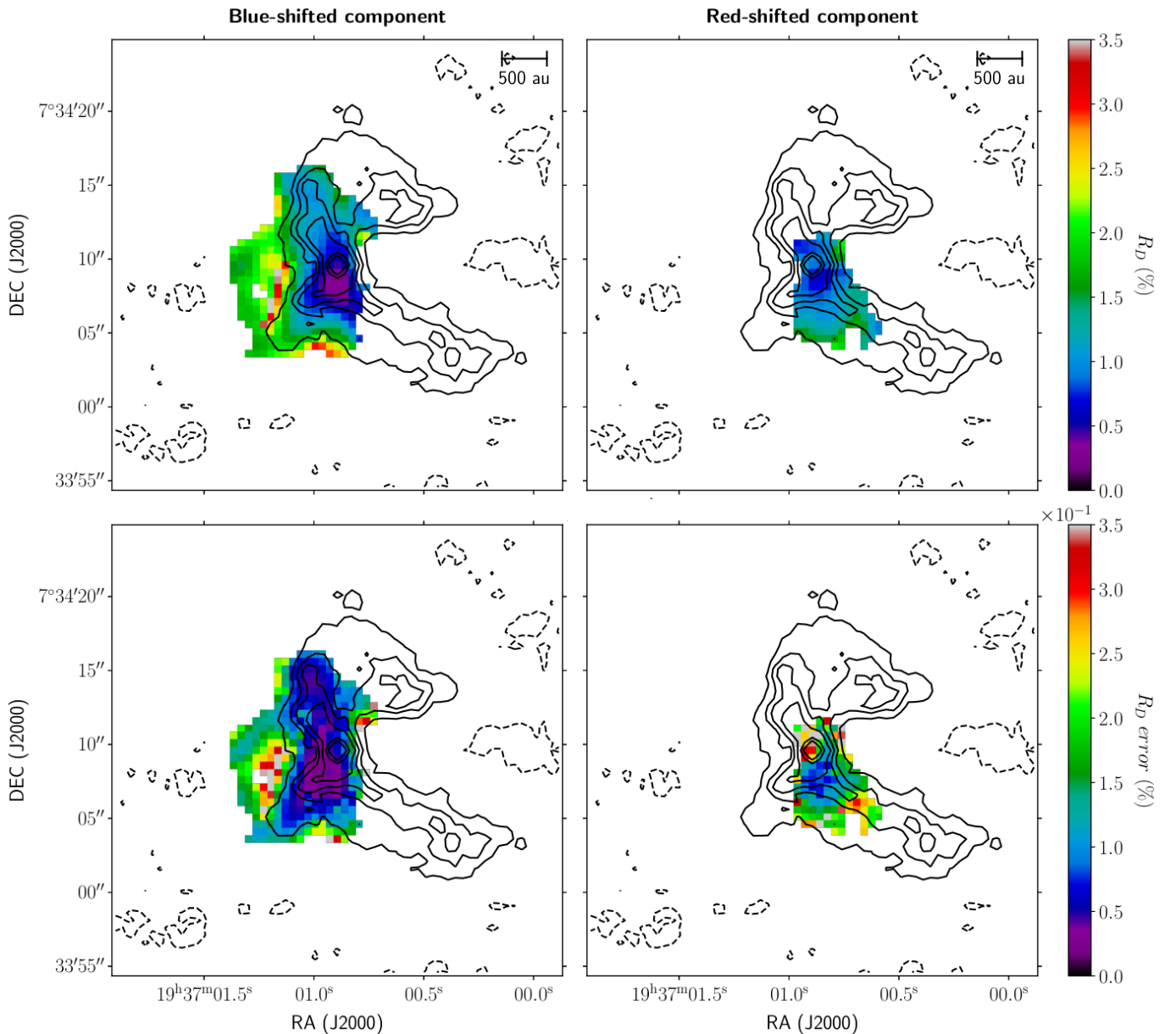


Fig. 2: Dust continuum emission at 110 GHz for $-2, 3, 5, 7, 10, 30, 50\sigma$ (black contours) superimposed on the deuterium fraction maps (top panels) and on the corresponding statistical uncertainties (lower panels) for the blue- and red-shifted velocity components (left and right column, respectively). The spatial scale is shown in the top-right corner of the upper panels.

not change significantly at these two temperatures with respect to the value adopted (25 K), the H^{13}CO^+ column density changes by about $\sim 15\%$. Nevertheless, the new values are still in agreement with the derived values of R_D from DCO^+ reported in the literature.

4. Ionization fraction and cosmic-ray ionization rate

We followed the method presented in Caselli et al. (1998) to compute the ionization fraction, χ_e , and the CR ionization rate, ζ , from R_D . The two quantities are given by

$$\chi_e = \frac{2.7 \times 10^{-8}}{R_D} - \frac{1.2 \times 10^{-6}}{f_D}, \quad (3)$$

and

$$\zeta = \left[7.5 \times 10^{-4} \chi_e + \frac{4.6 \times 10^{-10}}{f_D} \right] \chi_e n_{\text{H}_2} R_H, \quad (4)$$

where f_D is the depletion fraction of C and O, n_{H_2} is the H_2 volume density and R_H is the hydrogenation fraction, $R_H = [\text{HCO}^+]/[\text{CO}]$.

4.1. Estimate of the CO depletion in B335

Since the deuterium fraction, and therefore the ionization fraction, depend on the level of C and O depletion from the gas phase, we made the hypothesis that the CO abundance is proportional to the CO column density and estimated f_D as the ratio between the ‘expected’, $N_{\text{CO}}^{\text{exp}}$, and the ‘observed’ CO column

density, $N_{\text{CO}}^{\text{obs}}$:

$$f_{\text{D}} = \frac{N_{\text{CO}}^{\text{exp}}}{N_{\text{CO}}^{\text{obs}}}. \quad (5)$$

Here, $N_{\text{CO}}^{\text{exp}}$ is computed as the product of the H_2 column density, N_{H_2} , and the expected CO to H_2 abundance ratio, $X_{\text{CO}} = [\text{CO}]/[\text{H}_2] = 10^{-4}$ (Wilson & Rood 1994; Gerner et al. 2014), and $N_{\text{CO}}^{\text{obs}}$ is derived as the product between the C^{17}O column density, $N_{\text{C}^{17}\text{O}}$, and the C^{17}O to CO abundance ratio, $f_{\text{C}^{17}\text{O}} = [\text{CO}]/[\text{C}^{17}\text{O}] = 2317$ (Wouterloot et al. 2008). Then, the depletion factor is given by

$$f_{\text{D}} = \frac{N_{\text{H}_2} X_{\text{CO}}}{N_{\text{C}^{17}\text{O}} f_{\text{C}^{17}\text{O}}}. \quad (6)$$

The H_2 column density has been estimated from the dust thermal emission at 110 GHz (see Fig. 1) corrected for the primary beam attenuation. Indeed, N_{H_2} depends directly on the flux density measured on the continuum map, the beam solid angle Ω_{beam} , the Planck function $B_{\nu}(T_{\text{d}})$ at the dust temperature, and the dust mass opacity κ_{ν} (in units of $\text{cm}^2 \text{ g}^{-1}$) at the frequency of the dust thermal emission was observed:

$$N_{\text{H}_2} = -\frac{1}{\mu_{\text{H}_2} m_{\text{H}} \kappa_{\nu}} \ln \left[1 - \frac{S_{\nu}^{\text{beam}}}{\Omega_{\text{beam}} B_{\nu}(T_{\text{d}})} \right], \quad (7)$$

where $\mu_{\text{H}_2} = 2.8$, m_{H} is the atomic hydrogen mass, and for the dust opacity we used a power-law fit given by

$$\kappa_{\nu} = \frac{\kappa_0}{\chi_{\text{d}}} \left(\frac{\nu}{\nu_0} \right)^{\beta}. \quad (8)$$

We adopt a dust mass absorption coefficient $\kappa_0 = 1.6 \text{ cm}^2 \text{ g}^{-1}$ at $\lambda_0 = 1.3 \text{ mm}$, following Ossenkopf & Henning (1994). We assume a standard gas-to-dust ratio $\chi_{\text{d}} = 100$, a dust emissivity exponent $\beta = 0.76$ (Galametz et al. 2019), and a dust temperature $T_{\text{d}} = 25 \text{ K}$. The resulting N_{H_2} column densities probed in the ALMA dust continuum emission map range from $\sim 10^{20} \text{ cm}^{-2}$ at radii $\sim 1600 \text{ au}$ up to a few 10^{22} cm^{-2} at the protostar position. We note that the values of column density suffer from a systematic error due to assumptions on the parameters used to derive them (e.g. dust opacity, dust temperature). We estimate that the systematic error is about a factor of 3 to 5, being higher toward the peak position where standard dust properties and conditions of emission may not be met. We use Eq. 2 to estimate the observed CO column density $N_{\text{CO}} = N_{\text{C}^{17}\text{O}} f_{\text{C}^{17}\text{O}}$ from the C^{17}O emission map shown in Fig. 1, assuming an excitation temperature equal to the value used for the dust temperature, $T_{\text{ex}} = T_{\text{d}} = 25 \text{ K}$. The CO column density values are subject to systematic uncertainties due to the adopted gas temperature, as it is not well constrained and expected to vary across the envelope. Altogether, the systematic uncertainty is about a factor of 2, also higher toward the peak position where different gas temperatures are expected to be present along the line of sight.

Using Eq. 6, we obtain the CO depletion fraction map, shown in Fig. 3. The depletion factor ranges from ~ 20 in the outer regions to ~ 70 in the center of the object. Propagating the errors from the column density maps they stem from, we expect these depletion values are uncertain to a factor of 2 to 3, as the main source of errors, due to assumed gas and dust temperatures, are lessened by the ratio. The CO depletion seems highly asymmetric around the protostar, being the lowest in the south-eastern quadrant while high values are associated to the protostar position and the northern region. We note that the regions with high f_{D} coincide with the regions of low deuteration, shown in Fig. 2.

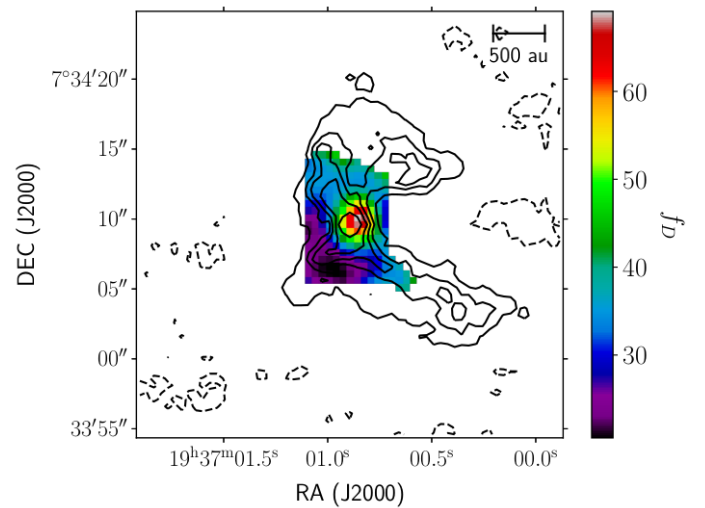


Fig. 3: Map of the CO depletion factor and contours of dust continuum emission at 110 GHz, for emission over 3σ . The spatial scale is shown in the top-right corner of the figure.

4.2. Ionization fraction of the gas

We obtained the ionization fraction of the gas using our deuteration fraction maps, shown in Sect. 3 and the CO depletion map, presented in Fig. 3. Top panels of Fig. 4 show the derived ionization fraction and the bottom panels the associated uncertainties, for the blue- and red-shifted velocity components (left and right column, respectively). We obtained a mean value of $\chi_{\text{e}} = 2 \times 10^{-6}$ for both components. Generally, these values are subject to statistical uncertainties of $\sim 1.5 \times 10^{-6}$. The range of values found for R_{D} and f_{D} indicates that the χ_{e} depends basically on the level of deuteration, hence the systematic error on the estimated ionization fraction of the gas from Eq. 3 are typically $< 30\%$ and statistical uncertainties dominate in this case. Since the deuteration fraction decreases toward the center of the source, we found that ionization increases toward the center.

4.3. Derivation of the CR ionization rate

We produced ionization rate maps using Eq. 4. We obtained n_{H_2} as N_{H_2}/L , using the N_{H_2} map obtained in Sect. 4.1 and considering a core diameter, L , of 1720 au, derived from the C^{17}O ($J=1-0$) emission (Cabedo et al. 2021). With this approximation, we find values of the volume density ranging from $\sim 10^4$ in the outer regions, to $\sim 10^6 \text{ cm}^{-3}$ at the protostar position. We obtained R_{H} for both velocity components as the column density ratio of H^{13}CO^+ ($J=1-0$) to C^{17}O ($J=1-0$), and accounting for $f_{12/13}\text{C}$ and $f_{\text{C}^{17}\text{O}}$:

$$R_{\text{H}} = \frac{N_{\text{H}^{13}\text{CO}^+} f_{12/13}\text{C}}{N_{\text{C}^{17}\text{O}} f_{\text{C}^{17}\text{O}}}. \quad (9)$$

Values of R_{H} are relatively uniform across the source, with mean values between 2 and 3×10^{-7} for the two velocity components. The statistical uncertainties of these values are generally one order of magnitude smaller than R_{H} .

The two terms within the brackets in Eq. 4 have values of the order of $\sim 10^{-9}$ and $\sim 10^{-11}$, respectively. Therefore, the derivation of the CR ionization rate is very sensitive to the ionization fraction but not to the CO depletion factor. Figure 5 shows in the top panels the derived CR ionization rate and in the bottom panels the associated statistical uncertainties, for the blue- and

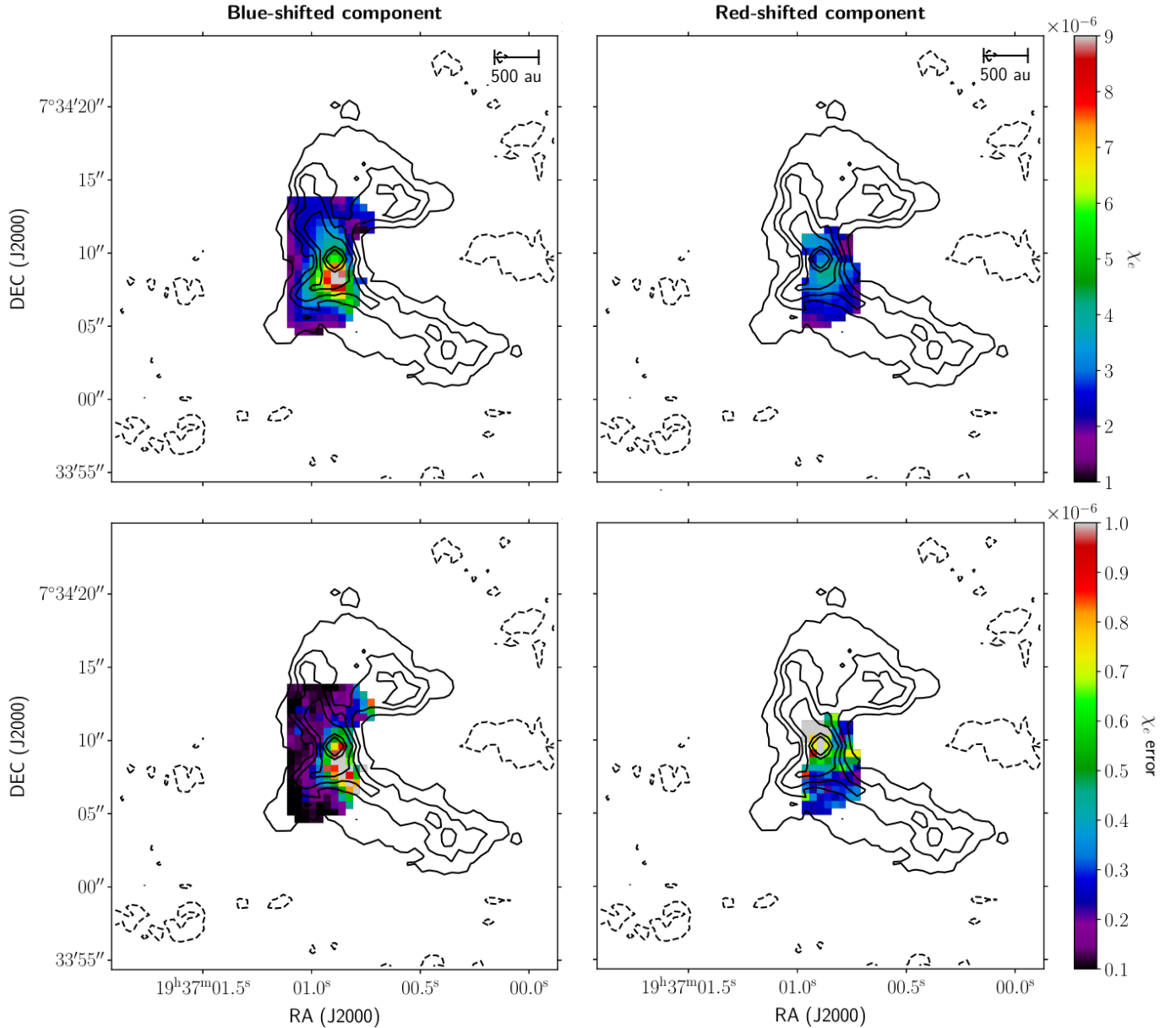


Fig. 4: Dust continuum emission at 110 GHz for $-2, 3, 5, 7, 10, 30, 50\sigma$ (black contours) superimposed on the ionization fraction maps (top panels) and on the corresponding statistical uncertainties (lower panels) for the blue- and red-shifted velocity components (left and right column, respectively). The spatial scale is shown in the top-right corner of the upper panels.

red-shifted velocity components (left and right column, respectively). As expected from the values of the ionization fraction, ζ increases toward the center, reaching values of $7 \times 10^{-14} \text{ s}^{-1}$ at the peak of the dust continuum. The uncertainties on ζ are large, due to all the errors coming from the modeling of the different molecules. Considering the systematic uncertainties on n_{H_2} and R_{H} we estimate the global uncertainty on the CR ionization rate values we find in B335 are of the same order of magnitude as the ζ values.

To interpret the trend of the ionization rate as a function of the distance from the density peak in an unbiased way, we considered profiles of ζ along directions from the density peak outwards denoted by the position angle ϑ , with $0 \leq \vartheta \leq \pi$ (see the lower right panel of Fig. 6). The envelope of the profiles is represented by the orange filled region in the upper left panel

of Fig. 6. Since the $\zeta(r, \vartheta)$ distributions between 40 and 700 au are skewed, for each radius \bar{r} we considered the median value of $\zeta(\bar{r}, \vartheta)$ and estimated the errors by using the first and third quartiles. We found that the trend of the ionization rate can be parameterised by two independent power-law profiles, $\zeta(r) \propto r^s$, with $s = -0.96 \pm 0.04$ and -3.77 ± 0.30 for radii smaller and larger than 270 au, respectively. The ionization rate decreases with radius following two very different trends. At $r < 270$ au, the slope is compatible with the diffusive regime (r^{-1}), then ζ drops abruptly.

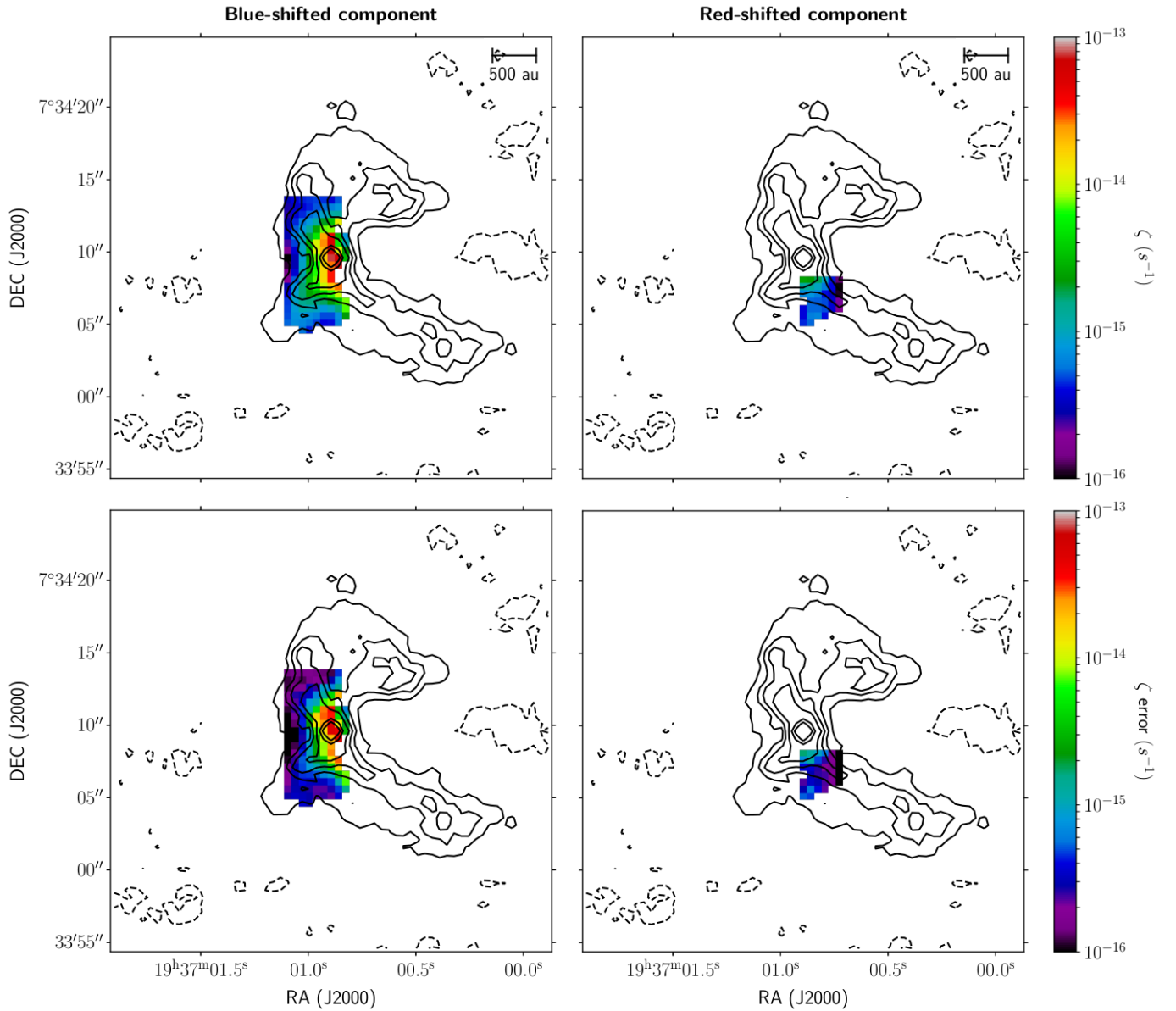


Fig. 5: Dust continuum emission at 110 GHz for $-2, 3, 5, 7, 10, 30, 50\sigma$ (black contours) superimposed on the ionization rate maps (top panels) and on the corresponding statistical uncertainties (lower panels) for the blue- and red-shifted velocity components (left and right column, respectively). The scale is shown in the top-right corner of the upper panels.

5. Discussion

5.1. Local destruction of deuterated molecules

The deuteration fractions observed in Class 0 protostars range between 1 and 10%, with a large scatter from source to source and at the different protostellar scales (Caselli 2002; Roberts et al. 2002; Jørgensen et al. 2004). The $[\mathrm{DCO}^+]/[\mathrm{H}^{13}\mathrm{CO}^+]$ values in B335 we find are thus in broad agreement with the typical range reported in the literature. However, Butner et al. (1995) found a $[\mathrm{DCO}^+]/[\mathrm{HCO}^+]$ of $\approx 3\%$ in B335 at scales of ~ 10000 au. This value is larger than the range of values we have found with ALMA at smaller scales, which indicates a decrease of the deuteration fraction toward the center of the envelope. Indeed, deuteration fraction decreases down to $< 1\%$ toward the center and the northern region of the source. This decrease could be attributed to local radiation processes occurring during the protostellar phase, after the protostar has been formed. An in-

crease in the local radiation could promote processes that would lead to the destruction of deuterated molecules due to the evaporation of neutrals to the gas phase (Caselli et al. 1998; Jørgensen et al. 2004), or the increased abundance of ionized molecules like HCO^+ (Gaches et al. 2019).

The decreasing trend in the deuteration fraction is further confirmed by our observations of $\mathrm{N}_2\mathrm{D}^+$ ($J=3-2$). Figure 7 shows the deuteration map overplotted with the $\mathrm{N}_2\mathrm{D}^+$ ($J=3-2$) integrated emission. A lack of $\mathrm{N}_2\mathrm{D}^+$ is observed in regions where the deuteration fraction is lower, suggesting that the physical processes lowering the abundance of O-bearing deuterated molecules also lower the abundance of N-bearing deuterated species, around the protostar.

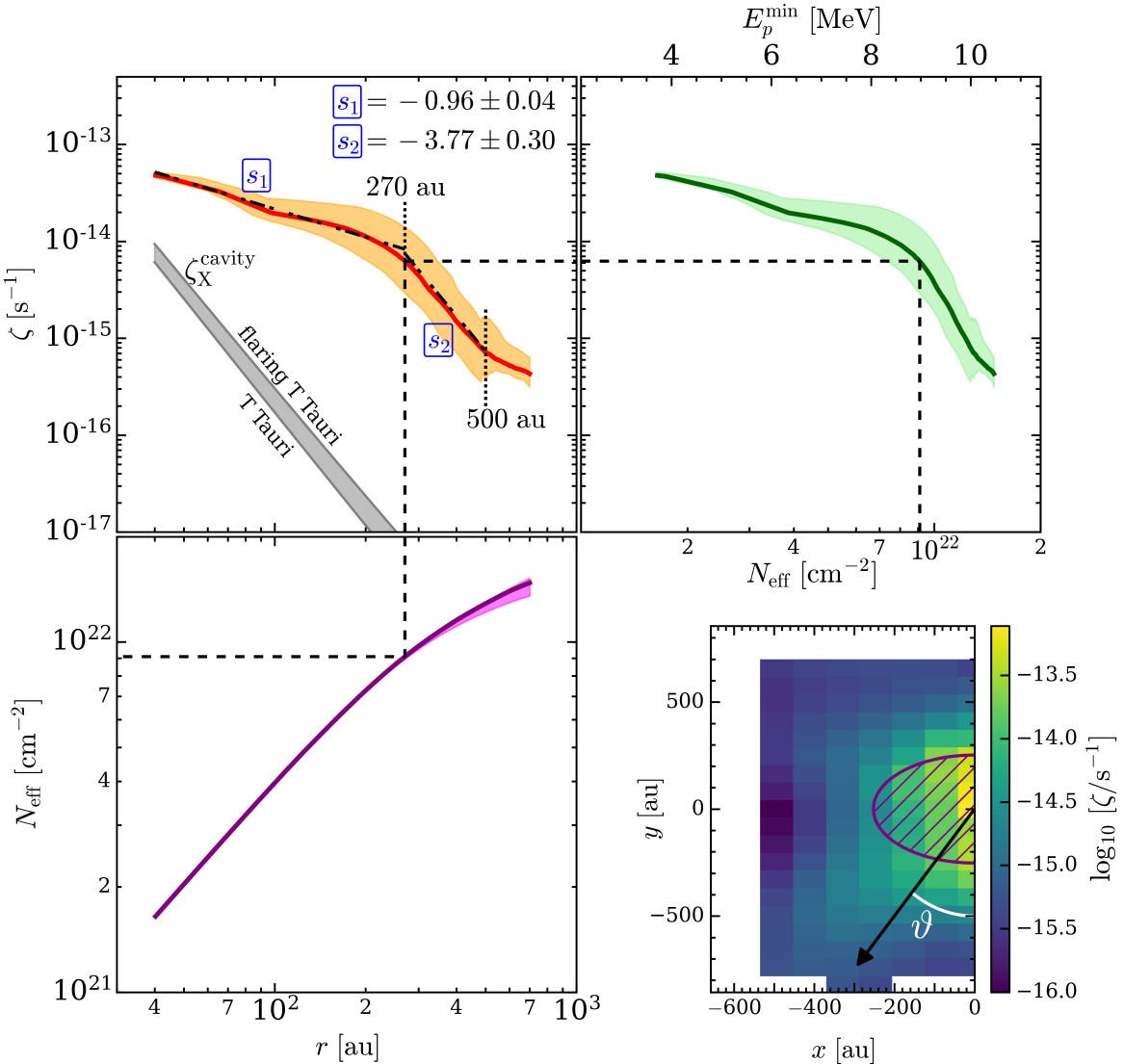


Fig. 6: *Upper left panel:* ionization rate, ζ , as a function of the radius, r . The two dotted black lines at 270 and 500 au identify the radius ranges used to compute the slopes (s_1 and s_2 , respectively). The grey shaded region shows the expected X-ray ionization in the outflow cavity for a typical and a flaring T Tauri star (Rab et al. 2017). *Lower left panel:* Effective column density, N_{eff} , accumulated by CRs and X-rays from the source centre outwards as a function of the radius. *Upper right panel:* ionization rate as a function of the effective column density. The upper x-axis shows the minimum energy that CR protons must have in order not to be thermalised (Padovani et al. 2018). The orange, magenta, and green filled regions in the three above panels represent the envelope of the ζ and N_{eff} profiles (see Sect. 5.2), while the red, purple, and dark green solid lines show their median value. *Lower right panel:* ionization rate map of the blue-shifted component (zoom of the upper left panel of Fig. 5) in logarithmic scale (coloured map). The purple hatched region shows a circle of radius 270 au, where CRs propagate according to the diffusive regime. For illustration purposes, the black arrow at the position angle ϑ shows a direction used to extract the ζ profile from the map. The black dashed lines identify the radius as well as the corresponding values of N_{eff} and ζ , where the slope of the ionization rate changes from s_1 to s_2 .

5.2. High C and O depletion values in the source

At core scales, observations of the depletion in B335 have been rather inconclusive as some studies suggested very little CO depletion (JCMT 20-arcsec beam probing 3000 au, Murphy et al. 1998), while others suggest a CO depletion of one order of magnitude, $f_D \sim 10$, at similarly large scales (Walmsley & Menten 1987). Our spatially resolved observations reveal large CO depletion values of the gas in the inner envelope of B335, at radii < 1000 au. As shown in Fig. 3 we find depletion factors ranging from 20 to 40 at radii 1000 to 100 au, except at the core center

where it increases up to 80. Such CO depletion at protostellar radii 100 – 1000 au is somehow unexpected, if one assumes depletion is due to freeze-out onto dust grains. Indeed, gas and dust at such radii should have temperatures beyond ~ 20 – 30 K, where the evaporation of CO from the surface of the dust should replenish it in the gas phase (Anderl et al. 2016). The high depletion values found at the protostellar position are highly uncertain due to unknown optical depth, and unconstrained dust and gas temperatures. We stress that the possible depletion increase toward the center in B335 should be confirmed with further observations of higher J transitions of CO.

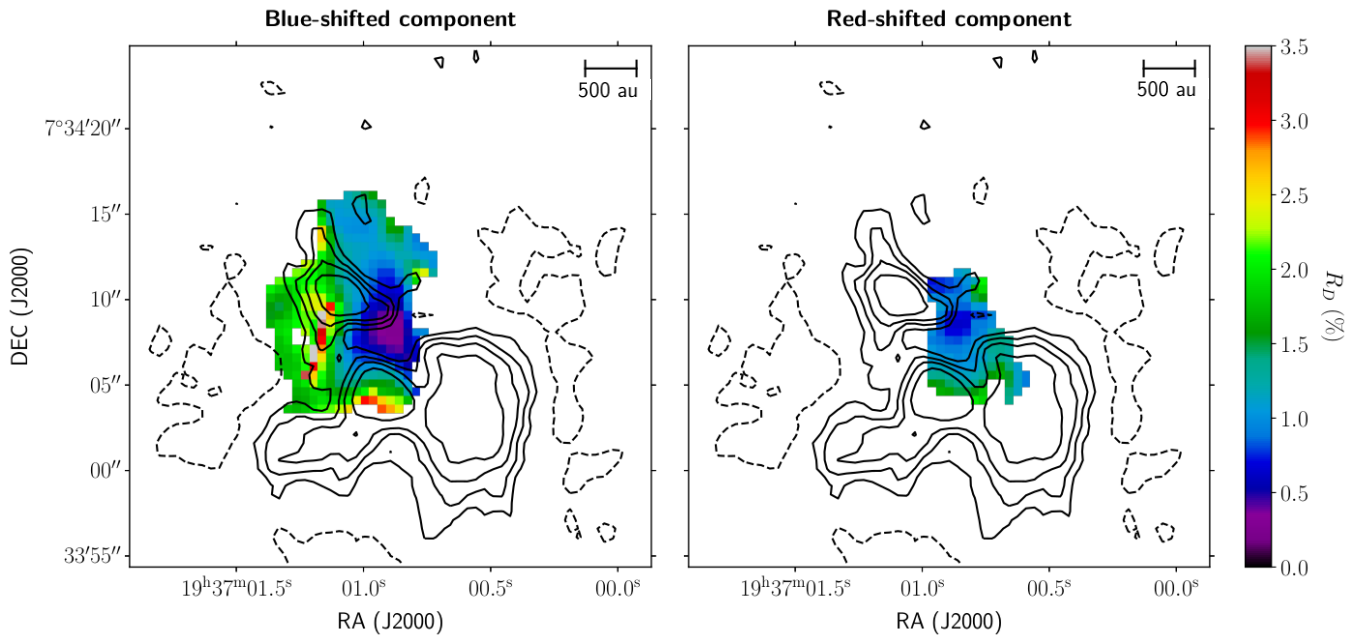


Fig. 7: N_2D^+ ($J=3-2$) emission in at 3, 5, 10, 15 and 20σ , where $\sigma = 5.23 \text{ mJy beam}^{-1}$ (black contours) and deuterium fraction maps for the blue- and red-shifted velocity components (left and right column, respectively). The spatial scale is shown in the top-right corners of each panel.

Several observational studies of protostellar cores have found depletion factors $f_D > 10$, at scales ~ 5000 au, with some spatially resolved studies pointing to values up to ~ 20 (Alonso-Albi et al. 2010; Christie et al. 2012; Yıldız et al. 2012; Fuente et al. 2012). Models of protostellar evolution with short warm-up timescales in the envelope (see e.g., Aikawa et al. 2012) show that the CO depletion factor may remain high even inside the sublimation radius, especially at early stages, because of the conversion of CO into CH_3OH and CH_4 on the grain surfaces. Photodissociation due to the protostellar UV radiation could contribute to lower the global CO abundance in the innermost layers of protostellar envelopes (Visser et al. 2009). Additionally, other sources of ionization, such as CRs, could decrease the abundance of CO in the gas phase by promoting its reaction for the formation of HCO^+ (Gaches et al. 2019). This decrease in CO by transformation into HCO^+ could also explain the observed coincidence between regions with large CO depletion and low R_D .

Another possible cause for the observed depletion could be the presence of relatively large dust grains, as observed in several protostars at similar scales by Galametz et al. (2019). Indeed, larger grains are less efficiently warmed up (Iqbal & Wakelam 2018), limiting the desorption of CO ices to the gas phase. Note that the presence of large dust grains in the inner envelope of B335 could also favor enhanced ionization of the gas (Walmsley et al. 2004), and thus also be consistent with our findings regarding ionization.

5.3. Origin of the ionization

From the single-dish observations of Butner et al. (1995), Caselli et al. (1998) find ionization fractions of protostellar gas at core scales of the order of 10^{-8} – 10^{-6} . In the B335 outer envelope where $n(\text{H}_2) \sim 10^4 \text{ cm}^{-3}$, they estimate χ_e of a few 10^{-6} . In the inner envelope, where $n(\text{H}_2) \sim 10^6 \text{ cm}^{-3}$, we measure an ioniza-

tion fraction of the gas χ_e around 2×10^{-6} , with the largest values being $\sim 9 \times 10^{-6}$. The large χ_e values could be produced by local UV and X-ray radiation produced in outflow shocks, altering the chemistry from the molecular content around the shocks (e.g., Viti & Williams 1999; Girart et al. 2002, 2005). However, ionization by far-UV (FUV) photons can be ruled out for two other reasons. The first is due to the fact that the maximum energy of FUV photons is around 13 eV, thus below the threshold for ionization of molecular hydrogen (15.44 eV). The second argument is related to the fact that the extinction cross section at FUV wavelengths ($\simeq 0.1 \mu\text{m}$) is $\sigma_{\text{UV}} \simeq 2 \times 10^{-21} \text{ cm}^2$ per hydrogen atom (Draine 2003). Thus, FUV photons are rapidly absorbed in a thin layer of column density equal to $(2\sigma_{\text{UV}})^{-1} \simeq 3 \times 10^{20} \text{ cm}^{-2}$.

The absorption cross section of X-ray photons, σ_X , in the range 1–10 keV is much smaller than at FUV frequencies (Bethell & Bergin 2011). For example, at 1 keV and 10 keV, $\sigma_X \simeq 2 \times 10^{-22} \text{ cm}^2$ and $\simeq 8 \times 10^{-25} \text{ cm}^2$ per H atom, respectively. While at 1 keV the corresponding absorption column density is still small, $(2\sigma_X)^{-1} \simeq 2 \times 10^{21} \text{ cm}^{-2}$, at 10 keV it reaches about $6 \times 10^{23} \text{ cm}^{-2}$, much larger than the maximum effective column density, N_{eff} , we found. The latter has been computed by integrating the dust continuum at 110 GHz along directions identified by the position angle ϑ (see lower right panel of Fig. 6) and is representative of the column density in the outflow cavity. We thus estimated the X-ray ionization rate, ζ_X , using the spectra described by Rab et al. (2017) for a typical and a flaring T Tauri star, assuming a stellar radius of $2R_\odot$. Results for ζ_X are shown in the upper left panel of Fig. 6. It is evident that X-ray ionization cannot explain the values of ζ estimated from observations. In addition, these values of ζ_X must be considered as an upper limit, since the exponential attenuation was taken into account assuming N_{eff} accumulated in the outflow cavity. However, a fraction of these X-ray photons ends up in the disk, which has much higher densities than the cavity, so N_{eff} can easily reach values greater than 10^{24} cm^{-2} , as found by Grossi et al. (2020)

for a Class 0 protostar. At such high N_{eff} , ζ_X decreases dramatically.

Once the high energy radiation field is excluded as the main source of the ionization rate estimated from observations, the only alternative left is CRs (see Sect. 4.3). However, the range of derived values is much higher than those expected from Galactic CRs (see Appendix C in Padovani et al. 2022, for an updated compilation of observational estimates of ζ). Following McKee (1989), $\chi_e = 1.3 \times 10^{-5} n(\text{H}_2)^{-1/2}$, and for the volume densities derived in Sect. 4.3, we should expect χ_e values of 10^{-7} to 10^{-8} , which are between one and two orders of magnitude lower than the observed values in B335. Since we also observed a significant increase of χ_e , and specially of ζ , toward the center, the origin of the high values should be of local origin. In particular, we are most likely witnessing the local acceleration of CRs in shocks located in B335 as predicted by theoretical models (Padovani et al. 2015, 2016, 2020). The values of ζ found in B335, between about 10^{-16} and 10^{-14} s^{-1} , are among the highest values reported in the literature toward star-forming regions (e.g. Maret & Bergin 2007; Ceccarelli et al. 2014b; Fuente et al. 2016; Fontani et al. 2017; Favre et al. 2017; Bialy et al. 2022). We stress that this is the first time that the CR ionization rate is measured at such small scales in a solar-type protostar and can be attributed to locally accelerated CRs, as well as the first time that a map of ζ is obtained.

There are two possible origins for the production of local CRs close to a protostar. One is in strong magnetized shocks along the outflow (Padovani et al. 2015, 2016; Fitz Axen et al. 2021; Padovani et al. 2021). Indeed, synchrotron radiation, which is the signature of the presence of relativistic electrons, has been detected in some outflows (Carrasco-González et al. 2010; Ainsworth et al. 2014; Rodríguez-Kamenetzky et al. 2016, 2019; Osorio et al. 2017). The second possibility is in accretion shocks near the stellar surface (Padovani et al. 2016; Gaches & Offner 2018). Both mechanisms are expected to generate low-energy CRs through the first-order Fermi acceleration mechanism with a rate of up to $\sim 10^{-13} \text{ s}^{-1}$.

The ionization rate slope found in B335 for $r < 270$ au is close to -1 and compatible with a diffusive regime, in agreement with predictions of theoretical models. Surprisingly, at radii larger than ~ 250 au, the slope decreases below -2 , thus beyond the geometrical dilution regime. We speculate on two possible explanations. On the one hand, local CRs may have accumulated enough column density to start being thermalized. On the other hand, at radii above about 250 au, both the dust emission and the ionization rate maps gradually lose their central symmetry (see Figs. 1 and 5, respectively). For example, the continuum map shows two higher density arms toward the northeast and southeast. Therefore, the slope, calculated by averaging over the position angle distribution ϑ , could be less than -2 . The loss of symmetry at larger radii in the ionization maps might also be an additional evidence as to the importance of non-symmetrical motions during the protostellar collapse (Cabedo et al. 2021). However, we note that these values are also affected by our limited angular resolution, 1.5 arcsec (~ 250 au), implying that only 3 or 4 points in the plot are completely independent, and that observations at larger angular resolution are needed in order to confirm the observed trend.

Previous observations indicate that B335 hosts a powerful and variable jet which might explain a large production of local CRs (Gálfalk & Olofsson 2007; Yen et al. 2010). Nevertheless, the exact origin of the local CR source is difficult to pinpoint due to our limited angular resolution. The effective column density calculated from the dust continuum map at 110 GHz (see lower

left panel of Fig. 6) is consistent with that expected in the outflow cavity. To calculate the minimum energy that protons must have in order to pass through a given column density without being thermalized, we can make use of the stopping range function (see Fig. 2 in Padovani et al. 2018). At $N_{\text{eff}} \simeq 10^{22} \text{ cm}^{-2}$, protons with energies of about 10 MeV are thermalized and lose their ionizing power (see also the upper x-axis of Fig. 6). As discussed above, if the shock is in the vicinity of the protostellar surface, an effective column density of the order of $10^{24} - 10^{25} \text{ cm}^{-2}$ can easily be accumulated (Grosso et al. 2020). In this case, the minimum proton energy required to prevent thermalization is 100 MeV and 400 MeV at 10^{24} and 10^{25} cm^{-2} , respectively. Models of local CR acceleration in low-mass protostars predict that accelerated protons can reach maximum energies of the order of 100 MeV and 10 GeV if the shock in which they are accelerated is located in the jet or close to the protostellar surface, respectively (Padovani et al. 2015, 2016). Thus, although the position of the shock that accelerates these local CRs in B335 is unknown, models suggest that the maximum energies of the protons are sufficiently high to explain the observed ionization.

Finally, we note that B335 has been observed to exhibit an organized magnetic field at scales similar to the ones probed here (Maury et al. 2018). This could also create favorable conditions for enhanced CR production.

5.4. Magnetic field coupling and non-ideal MHD effects

The ionization fraction of the gas in a young accreting protostar is not only important to understand the early chemistry around solar-type stars, feeding the scales where disks and planets will form. It is also the critical parameter that determines (i) the coupling between the magnetic field and the infalling-rotating gas in the envelope, and (ii) the role of diffusive processes, such as ambipolar diffusion, which counteract the outward transport of angular momentum due to magnetic fields (process known as magnetic braking). The higher the gas ionization, the more efficient the coupling, and the braking.

The large fraction of ionized gas unveiled by our observations in the inner envelope of B335 should lead to almost perfect coupling of the gas to the local magnetic field lines, generating a drastic braking of rotational motions. We note that these new results lend extra support to other observational evidence of a very efficient magnetic braking at work in B335: the highly pinched magnetic field lines observed at similar scales by Maury et al. (2018), and the failure to detect any disk larger than ~ 10 au in this object (Yen et al. 2015), although a new kinematic analysis may be motivated after the detection of several velocity components in the accreting gas at scales of ~ 500 au (Cabedo et al. 2021).

At the end of the pre-stellar stage, the fraction of ionized gas toward the central part of the core is expected to be very low as Galactic CRs do not penetrate deeply and there is no local ionization source (Padovani & Galli 2013; Ceccarelli et al. 2014a; Silsbee & Ivlev 2019). Hence, the initial stages of protostellar evolution are proceeding under low ionization conditions at typical $\zeta < 10^{-16} \text{ s}^{-1}$ (Padovani et al. 2018; Ivlev et al. 2019), which enhance the importance of non-ideal MHD processes (Padovani et al. 2014), with efficient diffusion of magnetic flux outwards during the very first phases of the collapse, and reduced magnetic braking. If the local ionization processes we observe in B335 are prototypical of solar-type Class 0 protostars, then CRs accelerated in the proximity of the protostar could be responsible for changing the ionization fraction of the gas at disk-forming scales once the protostar is formed, setting quasi-ideal MHD condi-

tions in the inner envelope. The timescale and magnitude of this transition from non-ideal MHD conditions to quasi-ideal MHD conditions may depend on the protostellar properties: more detailed modeling and observations toward other protostars are required to address this question. Moreover, we note that the observed large ionization fraction of the gas is not in agreement with the values used to calculate the simplified chemical networks in non-ideal MHD models of protostellar formation and evolution (Marchand et al. 2016; Zhao et al. 2020), as gas ionization is usually predicted from the gas density following McKee (1989). Thus, our observations suggest that a careful treatment of ionizing processes in magnetized models may be crucial to properly describe the gas-magnetic field coupling at different scales in embedded protostars.

In this scenario, the properties of protostellar disks could be tightly related to the local acceleration of low-energy CRs, and the development of a highly ionized region around the protostar. Thus, we would not expect the ionization fraction of the gas present at large-scale in the surrounding cloud to be a key factor in setting the disk properties, as proposed for example by Kuffmeier et al. (2020). The scenario we propose is also in agreement with recent ALMA observations of the Class II disks in Orion that do not find supporting evidence of local cloud properties affecting the disk properties (van Terwisga et al. 2022).

6. Conclusions and summary

This work provides new insights in the physico-chemical conditions of the gas in the young Class 0 protostar B335. For the first time, we derived a map of the gas ionization fraction and of the CR ionization rate at envelope scales < 1000 au in a Class 0 protostar. This allowed us to discuss the interplay between physical processes responsible for gas ionization at disk-forming scales, and its consequences on magnetized models of solar-type star formation. We summarize here the main results of our analysis:

- We used ALMA to obtain molecular line emission maps of B335 to characterize the ionization of the gas at envelope radii $\lesssim 1000$ au, and found large fractions of ionized gas, χ_e , between 1 and 8×10^{-6} . These values are remarkably higher than the ones usually measured at core scales.
- We produced for the first time a map of the CR ionization rate, ζ . Our map reveals very high values of ζ , between 10^{-16} and 10^{-14} s $^{-1}$, increasing at small envelope radii, toward the central protostellar embryo. This suggests that local acceleration of CRs, and not the penetration of interstellar CRs, may be responsible for the gas ionization in the inner envelope, potentially down to disk forming scales.
- The large fraction of ionized gas we find suggests an efficient coupling between the magnetic field and the gas in the inner envelope of B335. This interpretation is also supported by the observations of highly organized magnetic field lines, and no detection of a large rotationally-supported disk in B335.

If our findings are found to be prototypical of the low-mass star formation process, they might imply that the collapse at scales < 1000 au transitions from non-ideal to a quasi-ideal MHD once the central protostar starts ionizing its surrounding gas, and very efficient magnetic braking of the rotating-infalling protostellar gas might then take place. Protostellar disk properties may thus be determined by local processes setting the magnetic field coupling, and not only by the amount of angular momentum available at large envelope scales and by the magnetic

field strength in protostellar cores. We stress that the gas ionization we find in B335 significantly stands out from the typical values routinely used in state-of-the-art models of protostellar formation and evolution. Our observations suggest that a careful treatment of ionizing processes in these magnetized models may be crucial to properly describe the processes responsible for disk formation and early evolution. We also note that more observations of B335 at higher spatial resolution, and of other Class 0 protostars are crucial to confirm our results.

Acknowledgments

This project has received funding from the European Research Council (ERC) under the European Union Horizon 2020 research and innovation programme (MagneticYSOs project, grant agreement N° 679937). This work was also partially supported by the program Unidad de Excelencia María de Maeztu CEX2020-001058-M. JMG also acknowledges support by the grant PID2020-117710GB-I00 (MCI-AEI-FEDER,UE).

Additionally, this paper makes use of the following ALMA data: 2015.1.01188.S. ALMA is a partnership of ESO (representing its member states), NSF (USA) and NINS (Japan), together with NRC (Canada), MOST and ASIAA (Taiwan), and KASI (Republic of Korea), in cooperation with the Republic of Chile. The Joint ALMA Observatory is operated by ESO, AUI/NRAO and NAOJ

References

Aikawa, Y., Wakelam, V., Hersant, F., Garrod, R. T., & Herbst, E. 2012, ApJ, 760, 40
 Ainsworth, R. E., Scaife, A. M. M., Ray, T. P., et al. 2014, ApJ, 792, L18
 Alonso-Albi, T., Fuente, A., Crimier, N., et al. 2010, A&A, 518, A52
 Alves, F. O., Frau, P., Girart, J. M., et al. 2014, A&A, 569, L1
 Anderl, S., Maret, S., Cabrit, S., et al. 2016, A&A, 591, A3
 Asayama, S., Biggs, A., de Gregorio, I., et al. 2016, ALMA Partnership
 Bethell, T. J. & Bergin, E. A. 2011, ApJ, 740, 7
 Bialy, S., Belli, S., & Padovani, M. 2022, A&A, 658, L13
 Butner, H. M., Lada, E. A., & Loren, R. B. 1995, ApJ, 448, 207
 Cabedo, V., Maury, A., Girart, J. M., & Padovani, M. 2021, A&A, 653, A166
 Carrasco-González, C., Rodríguez, L. F., Anglada, G., et al. 2010, Science, 330, 1209
 Caselli, P. 2002, Planet. Space Sci., 50, 1133
 Caselli, P., Walmsley, C. M., Terzieva, R., & Herbst, E. 1998, ApJ, 499, 234
 Ceccarelli, C., Caselli, P., Bockelée-Morvan, D., et al. 2014a, in Protostars and Planets VI, ed. H. Beuther, R. S. Klessen, C. P. Dullemond, & T. Henning, 859
 Ceccarelli, C., Dominik, C., López-Sepulcre, A., et al. 2014b, ApJ, 790, L1
 Christie, H., Viti, S., Yates, J., et al. 2012, MNRAS, 422, 968
 Dapp, W. B., Basu, S., & Kunz, M. W. 2012, A&A, 541, A35
 Draine, B. T. 2003, ARA&A, 41, 241
 Estalella, R. 2017, PASP, 129, 025003
 Evans, Neal J., I., Di Francesco, J., Lee, J.-E., et al. 2015, ApJ, 814, 22
 Favre, C., López-Sepulcre, A., Ceccarelli, C., et al. 2017, A&A, 608, A82
 Fitz Axen, M., Offner, S. S. S., Gaches, B. A. L., et al. 2021, ApJ, 915, 43
 Fontani, F., Ceccarelli, C., Favre, C., et al. 2017, A&A, 605, A57
 Fuente, A., Caselli, P., McCoey, C., et al. 2012, A&A, 540, A75
 Fuente, A., Cernicharo, J., Roueff, E., et al. 2016, A&A, 593, A94
 Gaches, B. A. L. & Offner, S. S. R. 2018, ApJ, 861, 87
 Gaches, B. A. L., Offner, S. S. R., & Bisbas, T. G. 2019, ApJ, 878, 105
 Galametz, M., Maury, A. J., Valdivia, V., et al. 2019, A&A, 632, A5
 Gálfalk, M. & Olofsson, G. 2007, A&A, 475, 281
 Gerner, T., Beuther, H., Semenov, D., et al. 2014, A&A, 563, A97
 Girart, J. M., Rao, R., & Marrone, D. P. 2006, Science, 313, 812
 Girart, J. M., Viti, S., Estalella, R., & Williams, D. A. 2005, A&A, 439, 601
 Girart, J. M., Viti, S., Williams, D. A., Estalella, R., & Ho, P. T. P. 2002, A&A, 388, 1004
 Grosso, N., Hamaguchi, K., Principe, D. A., & Kastner, J. H. 2020, A&A, 638, L4
 Hennebelle, P., Commerçon, B., Lee, Y.-N., & Charnoz, S. 2020, A&A, 635, A67

Hennebelle, P. & Inutsuka, S.-i. 2019, *Frontiers in Astronomy and Space Sciences*, 6, 5

Hirano, N., Kameya, O., Kasuga, T., & Umemoto, T. 1992, *ApJ*, 390, L85

Hirano, N., Kameya, O., Nakayama, M., & Takakubo, K. 1988, *ApJ*, 327, L69

Iqbal, W. & Wakelam, V. 2018, *A&A*, 615, A20

Ivlev, A. V., Silsbee, K., Sipilä, O., & Caselli, P. 2019, *ApJ*, 884, 176

Jørgensen, J. K., Schöier, F. L., & van Dishoeck, E. F. 2004, *A&A*, 416, 603

Keene, J., Davidson, J. A., Harper, D. A., et al. 1983, *ApJ*, 274, L43

Kuffmeier, M., Zhao, B., & Caselli, P. 2020, *A&A*, 639, A86

Kurono, Y., Saito, M., Kamazaki, T., Morita, K.-I., & Kawabe, R. 2013, *ApJ*, 765, 85

Lebreuilly, U., Hennebelle, P., Colman, T., et al. 2021, *ApJ*, 917, L10

Li, Z.-Y., Krasnopol'sky, R., & Shang, H. 2011, *ApJ*, 738, 180

Machida, M. N., Inutsuka, S.-I., & Matsumoto, T. 2011, *PASJ*, 63, 555

Marchand, P., Masson, J., Chabrier, G., et al. 2016, *A&A*, 592, A18

Marchand, P., Tomida, K., Tanaka, K. E. I., Commerçon, B., & Chabrier, G. 2020, *ApJ*, 900, 180

Maret, S. & Bergin, E. A. 2007, *ApJ*, 664, 956

Masson, J., Chabrier, G., Hennebelle, P., Vaytet, N., & Commerçon, B. 2016, *A&A*, 587, A32

Maury, A. J., André, P., Testi, L., et al. 2019, *A&A*, 621, A76

Maury, A. J., Girart, J. M., Zhang, Q., et al. 2018, *MNRAS*, 477, 2760

McKee, C. F. 1989, *ApJ*, 345, 782

Murphy, B. T., Little, L. T., & Kelly, M. L. 1998, *MNRAS*, 294, 635

Osorio, M., Díaz-Rodríguez, A. K., Anglada, G., et al. 2017, *ApJ*, 840, 36

Ossenkopf, V. & Henning, T. 1994, *A&A*, 291, 943

Padovani, M., Bialy, S., Galli, D., et al. 2022, *arXiv e-prints*, arXiv:2201.08457

Padovani, M. & Galli, D. 2013, in *Astrophysics and Space Science Proceedings*, Vol. 34, *Cosmic Rays in Star-Forming Environments*, ed. D. F. Torres & O. Reimer, 61

Padovani, M., Galli, D., Hennebelle, P., Commerçon, B., & Joos, M. 2014, *A&A*, 571, A33

Padovani, M., Hennebelle, P., Marcowith, A., & Ferrière, K. 2015, *A&A*, 582, L13

Padovani, M., Ivlev, A. V., Galli, D., & Caselli, P. 2018, *A&A*, 614, A111

Padovani, M., Ivlev, A. V., Galli, D., et al. 2020, *Space Sci. Rev.*, 216, 29

Padovani, M., Marcowith, A., Galli, D., Hunt, L. K., & Fontani, F. 2021, *A&A*, 649, A149

Padovani, M., Marcowith, A., Hennebelle, P., & Ferrière, K. 2016, *A&A*, 590, A8

Rab, C., Güdel, M., Padovani, M., et al. 2017, *A&A*, 603, A96

Roberts, H., Fuller, G. A., Millar, T. J., Hatchell, J., & Buckle, J. V. 2002, *A&A*, 381, 1026

Rodríguez-Kamenetzky, A., Carrasco-González, C., Araudo, A., et al. 2016, *ApJ*, 818, 27

Rodríguez-Kamenetzky, A., Carrasco-González, C., González-Martín, O., et al. 2019, *MNRAS*, 482, 4687

Silsbee, K. & Ivlev, A. V. 2019, *ApJ*, 879, 14

Soler, J. D. 2019, *A&A*, 629, A96

Stutz, A. M., Rubin, M., Werner, M. W., et al. 2008, *ApJ*, 687, 389

Thomas, H. S. & Fuller, G. A. 2008, *A&A*, 479, 751

van Terwisga, S. E., Hacar, A., van Dishoeck, E. F., Oonk, R., & Portegies Zwart, S. 2022, *arXiv e-prints*, arXiv:2202.11057

Visser, R., van Dishoeck, E. F., & Black, J. H. 2009, *A&A*, 503, 323

Viti, S. & Williams, D. A. 1999, *MNRAS*, 310, 517

Walmsley, C. M., Flower, D. R., & Pineau des Forêts, G. 2004, *A&A*, 418, 1035

Walmsley, C. M. & Menten, K. M. 1987, in *Circumstellar Matter*, ed. I. Appenzeller & C. Jordan, Vol. 122, 71

Watson, D. M. 2020, *Research Notes of the American Astronomical Society*, 4, 88

Wilson, T. L. & Rood, R. 1994, *ARA&A*, 32, 191

Wouterloot, J. G. A., Henkel, C., Brand, J., & Davis, G. R. 2008, *A&A*, 487, 237

Yen, H.-W., Takakuwa, S., Koch, P. M., et al. 2015, *ApJ*, 812, 129

Yen, H.-W., Takakuwa, S., & Ohashi, N. 2010, *ApJ*, 710, 1786

Yıldız, U. A., Kristensen, L. E., van Dishoeck, E. F., et al. 2012, *A&A*, 542, A86

Zhang, Q., Qiu, K., Girart, J. M., et al. 2014, *ApJ*, 792, 116

Zhao, B., Caselli, P., Li, Z.-Y., et al. 2020, *MNRAS*, 492, 3375

Zhou, S., Evans, Neal J., I., Koempe, C., & Walmsley, C. M. 1993, *ApJ*, 404, 232

Appendix A: Technical details of the ALMA observations

Table A.1 presents the technical details of the ALMA observations presented in this work, including the ALMA configuration,

the date and time-range, the central frequency, the obtained spectral resolution and the different calibrators used.

Appendix B: Line profile analysis

B.1. Spectral maps

The DCO^+ (J=3-2) and H^{13}CO^+ (J=3-2) spectral maps are presented in Figs. B.1 and B.3. Both maps show emission in a region of $5.5'' \times 5.5''$ (900 au) around the center of the source, with each spectrum corresponding to a pixel of $0.5''$ (82 au). The H^{13}CO^+ (J=1-0) shows only a region $4'' \times 4''$ (685 au) and each spectrum corresponds to $0.25''$ (41 au).

The three tracers present the same pattern observed in C^{17}O (J=1-0), presented in Cabedo et al. (2021). The line profiles are double-peaked with one of the two velocity components progressively disappearing at different offsets of the source, i.e., the blue-shifted component is dominant in the eastern region of the source while the red-shifted component is present only in the western region. For the three transitions, the blue-shifted component is always more intense than the red-shifted one which produces the blue asymmetric morphology observed in the integrated intensity images.

Since none of the tracers presents a morphology typical of the outflow cavity, we assume that they are not tracing outflowing gas and that the two velocity components are not caused by this effect. This is confirmed with the spectral maps where no signatures coming from outflowing gas, such as very broad lines or high velocity wings, can be observed in the line profiles. This is generally true, except for a small region on the south-east region of the H^{13}CO^+ (J=3-2) map, where an additional third velocity component, or a "shoulder" can be observed. This additional component appears to be very broad, and at velocities of $\sim 7.6 - 7.7 \text{ km s}^{-1}$. We do attribute this signature to outflow contamination, which is not observed neither in DCO^+ (J=3-2) or in H^{13}CO^+ (J=1-0). We consider that while the outflow might have some effect in the line profiles, this is negligible and is not the main cause of the double-peaked line profiles. The effect of large scale filtering can not be ruled out. This is particularly visible in the DCO^+ (J=3-2) and H^{13}CO^+ (J=3-2) where negative emission is observed in the center and west regions of the source. While these two effects can be a source of uncertainty in our analysis, we conclude that they alone cannot produce the observed line profiles and the velocity pattern through the source, and proceed with the line modeling with the assumption of two independent velocity components.

B.2. Line profile modeling

In this case, since none of the transitions present a resolved hyperfine structure, the opacity of the line could not be obtained by modeling of the line profile and only the peak velocity and velocity dispersion maps (as σ) are presented. The resulting maps for DCO^+ (J=3-2), H^{13}CO^+ (J=1-0) and H^{13}CO^+ (J=3-2) are shown in Figs. B.4, B.5 and B.6. For the three tracers, the two separated velocity components occupy different regions of the source, indicating that they are probing gas with different motions. The morphology of the two components is similar for the three tracers, however, it is slightly different than for the C^{17}O (Fig. 5 in Cabedo et al. 2021), where the red-shifted component extends to a largest part of the integrated emission.

Peak velocity values (top panels of Figs. B.4, B.5 and B.6) ranges are similar for all molecules (from ~ 8 to 9 km s^{-1}), although the blue-shifted component goes to slightly lower veloc-

Table A.1: Technical details of the ALMA observations.

Config.	Date (mm/dd/yy)	Timerange (hh:min:s.ms; UTC)	Center freq. (GHz)	Spec. Res. (km s ⁻¹)	Flux cal.	Phase cal.	Bandpass cal.
C40-1	19/03/2017	10:40:52.8 - 10:53:42.8	231.0	0.09	J1751+0939	J1851+0035	J1751+0939
C40-2	02/07/2017	15:30:38.9 - 15:49:59.2	110.0	0.08	J1751+0939	J1938+0448	J1751+0939
C40-3	12/06/2016	18:39:47.5 - 19:24:24.3	87.7	0.1	J1751+0939	J1938+0448	J1751+0939
C40-4	21/11/2016	22:41:22.0 - 23:28:19.8	231.0	0.09	J2148+0657	J1851+0035	J2148+0657
C40-5	10/22/2016 - 10/23/2016	23:34:05.4 - 00:02:51.3	110.0	0.08	J2148+0657	J1938+0448	J2025+3343
	10/10/2016	20:50:38.0 - 21:39:40.2	87.7	0.1	J1751+0939	J1938+0448	J1751+0939
	10/10/2016	22:43:07.4 - 23:24:00.4	87.7	0.1	J1751+0939	J1938+0448	J1751+0939
	10/11/2016	21:14:59.4 - 22:03:55.2	87.7	0.1	J1751+0939	J1938+0448	J1751+0939

ities for H¹³CO⁺ (J=3-2), being the lowest velocities ~ 7.8 km s⁻¹. This decrease occurs toward the south-eastern region of the core, at $\sim 5''$ from the center. We attribute this to the presence of the third velocity component produced by outflow contamination observed in Fig. B.3, which produces a bad model of the line profile. No gradient indicating rotation is observed in the velocity maps for any tracer.

Velocity dispersion (bottom panels of Figs. B.4, B.5 and B.6) ranges are also similar for all tracers (from 0.1 to 0.5 km s⁻¹). However, there are some main differences: velocity dispersion is generally larger for H¹³CO⁺ (J=3-2) with average values of ~ 0.4 km s⁻¹, whereas for DCO⁺ (J=3-2) and H¹³CO⁺ (J=1-0) mean values are around ~ 0.25 km s⁻¹. Very large values of the velocity dispersion (>0.5 km s⁻¹) are observed in the same south-eastern region of the blue-shifted component of H¹³CO⁺ (J=3-2) consequence of the poor fitting due to the third velocity component. Values for the velocity dispersion are generally larger for the blue- than for the red-shifted velocity component indicating the two components trace gas with different kinematics, i.e., different infall velocities or are affected differently by turbulence. For all tracers and both velocity components, the velocity dispersion increases toward the center, as the temperature rises. This increase is smaller for the H¹³CO⁺ (J=1-0) emission (up to ~ 0.35 km s⁻¹) than for the DCO⁺ (J=3-2) and H¹³CO⁺ (J=3-2) (up to ~ 0.5 km s⁻¹) indicating that H¹³CO⁺ (J=1-0) traces gas at colder temperatures and further to the center of the source.

In general, there is a good agreement between the values obtained for DCO⁺ (J=3-2) and H¹³CO⁺ (J=3-2), both for peak velocity and velocity components. Considering that we are tracing similar scales, this confirms that both tracers are tracing similar gas. However, C¹⁷O presents some differences with respect to H¹³CO⁺ (J=1-0) which indicates that they are tracing slightly different gas, C¹⁷O tracing warmer and denser gas closer to the protostar.

Appendix C: Estimation of the opacity effects

Since the line profile modeling does not allow us to obtain the line opacities, we estimated the optical depth using the dust continuum emission and the molecular abundances, in order to determine what is its impact in the parameters derived from the line modeling. We first compute the H₂ column density map from the dust continuum emission map at 110 GHz (shown in Fig. 1), assuming its emission is optically thin e.g., tracing the full column density, and applying the following standard abundances: [C¹⁷O] = 5×10^{-8} (Thomas & Fuller 2008), [DCO⁺] = 10^{-11} and [H¹³CO⁺] = 10^{-10} (Jørgensen et al. 2004). Figure C.1 shows the expected optical depth maps for the four different molecular

lines we obtain with this method. Values of the optical depth are generally low (< 1), although they increase to larger values for all tracers in the central beam. We note that since we are considering a constant temperature for the derivation of the H₂ column density, which is likely higher at the center, the H₂ column density values in the central compact source are probably smaller, and we are overestimating the optical depth in that region. It can be seen that both transitions of H¹³CO⁺ present larger values of optical depth than both C¹⁷O (J=1-0) and DCO⁺ (J=3-2). We acknowledge that these large values can potentially affect our deuteration measurements toward the central beam, but stress that the small optical depth values found in DCO⁺ confirm that the two velocity components are not mainly produced by self-absorption effects. Outside of that central beam, the expected line opacities are generally smaller than 1, so we found no need of applying an opacity correction to our data.

DCO⁺ (3-2)

Fig. B.1: Spectral map of the DCO⁺ (J=3-2) emission in the inner 900 au, centered on the dust continuum emission peak. The whole map is $5.5'' \times 5.5''$ and each pixel correspond to $0.5''$ (~ 82 au). The red spectrum refers to the peak of the continuum emission and the blue line indicates the systemic velocity (8.3 km s $^{-1}$)

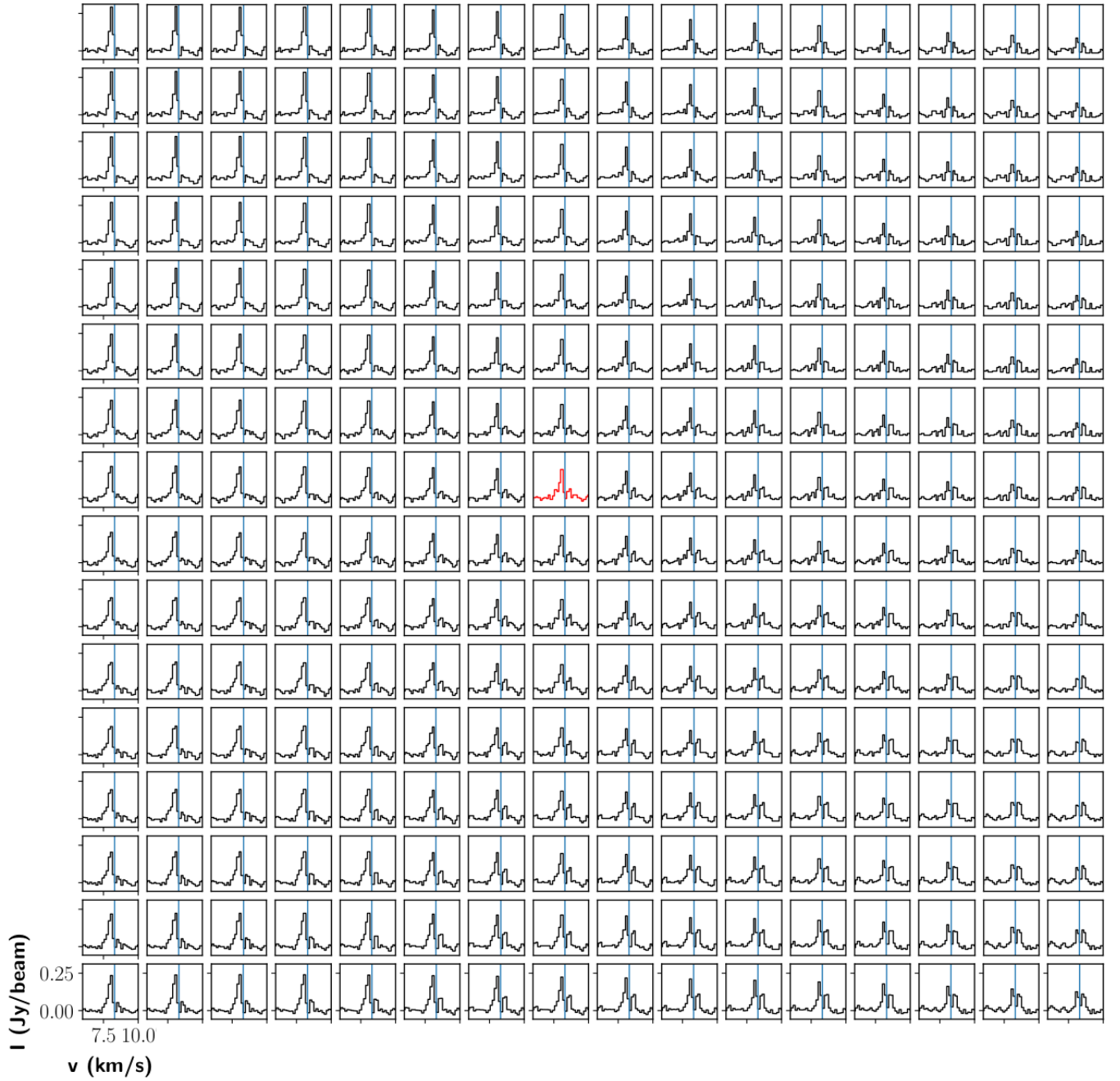
$\text{H}^{13}\text{CO}^+ (1-0)$ 

Fig. B.2: Spectral map of the H^{13}CO^+ (J=1-0) emission in the inner 658 au, centered on the dust continuum emission peak. The whole map is $4'' \times 4''$ and each pixel correspond to $0.25''$ (~ 41 au). The red spectrum refers to the peak of the continuum emission and the blue line indicates the systemic velocity (8.3 km s^{-1}).

$\text{H}^{13}\text{CO}^+ (3-2)$ 

Fig. B.3: Spectral map of the H^{13}CO^+ ($J=3-2$) emission in the inner 900 au, centered on the dust continuum emission peak. The whole map is $5.5'' \times 5.5''$ and each pixel correspond to $0.5''$ (~ 82 au). The red spectrum refers to the peak of the continuum emission and the blue line indicates the systemic velocity (8.3 km s^{-1})

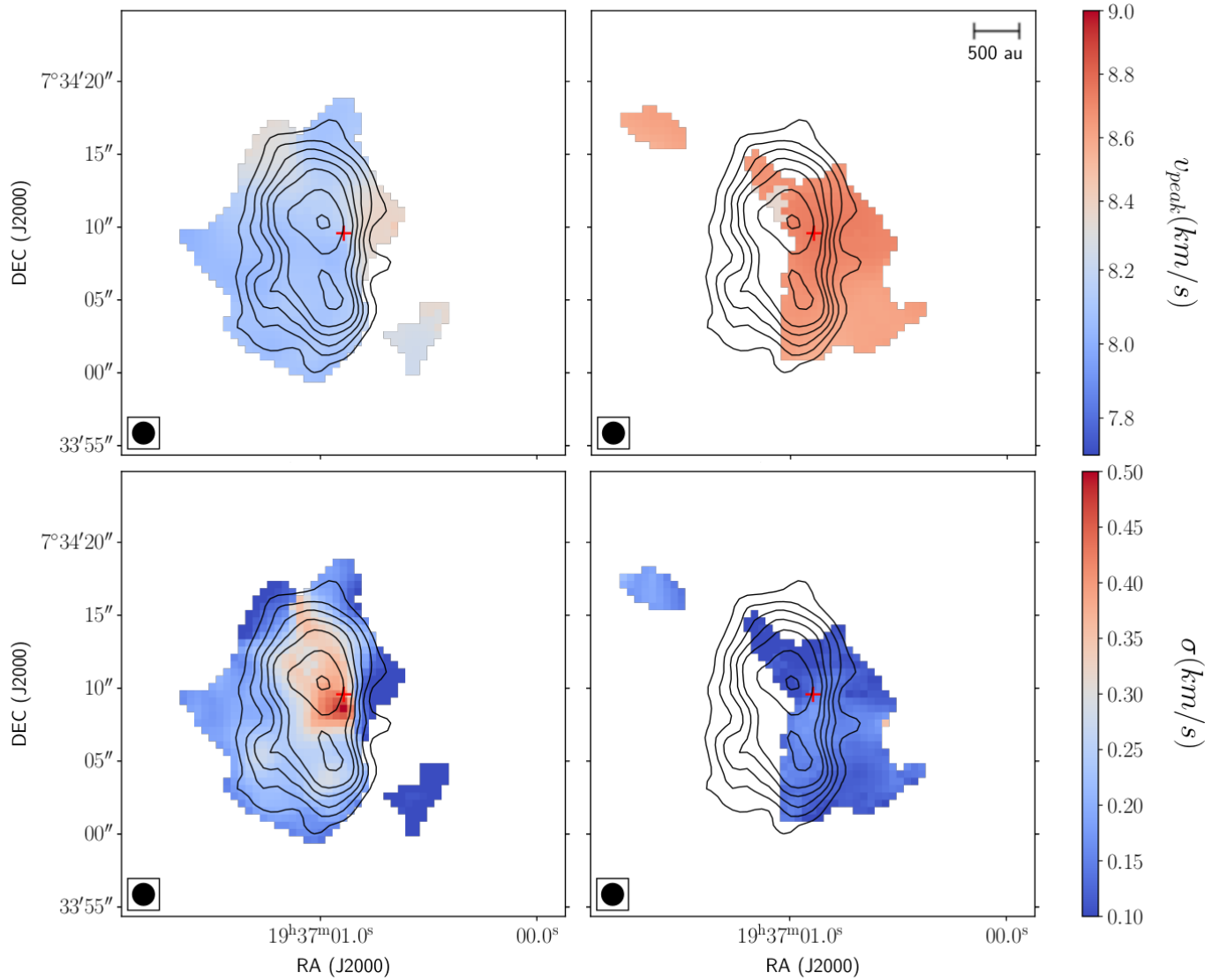


Fig. B.4: DCO⁺ (J=3-2) maps obtained from modeling the line profiles with two velocity components. Overlaid contours show the integrated intensity at -3, 3, 5, 10 and 20 σ . Top map shows values for the peak velocity and bottom show values for the linewidth (given as σ). Left and right show the blue- and red-shifted component respectively.

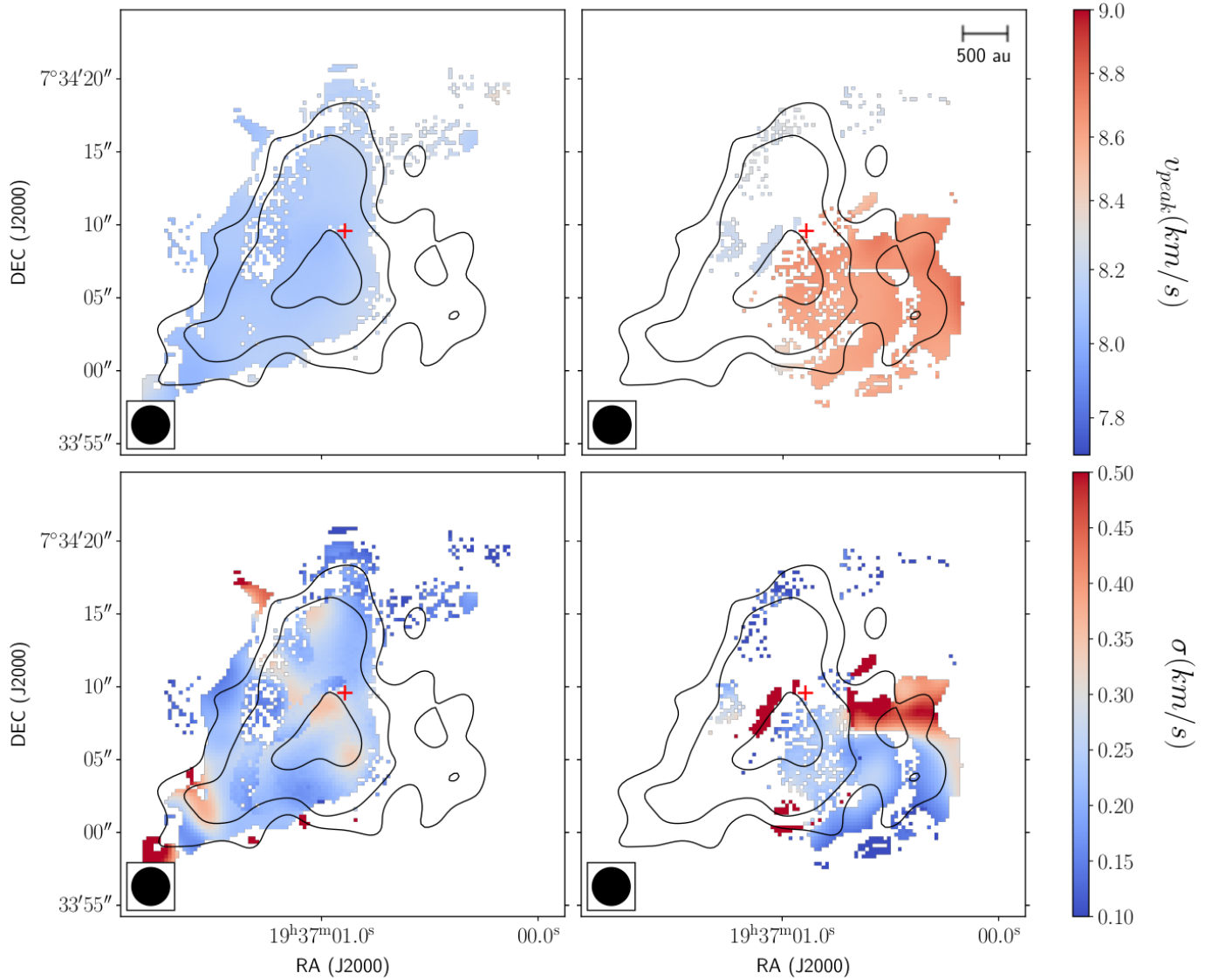


Fig. B.5: H^{13}CO^+ (J=1-0) maps obtained from modeling the line profiles with two velocity components. Overlaid contours show the integrated intensity at -3, 3, 5 and 10 σ . Top map shows values for the peak velocity and bottom show values for the linewidth (given as σ). Left and right show the blue- and red-shifted component respectively.

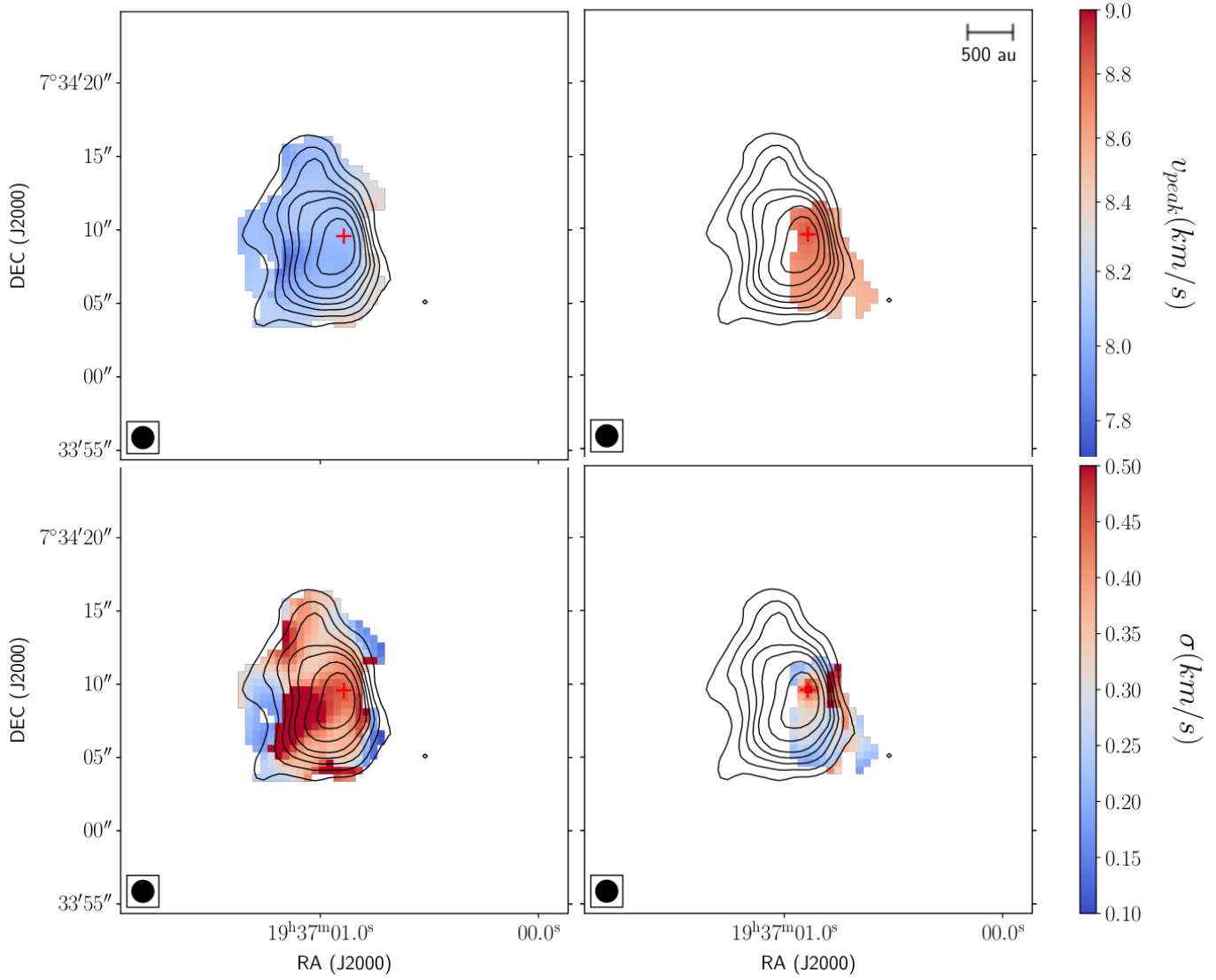


Fig. B.6: H^{13}CO^+ (J=3-2) maps obtained from modeling the line profiles with two velocity components. Overlaid contours show the integrated intensity at -3, 3, 5, 10 and 20 σ . Top map shows values for the peak velocity and bottom show values for the linewidth (given as σ). Left and right show the blue- and red-shifted component respectively.

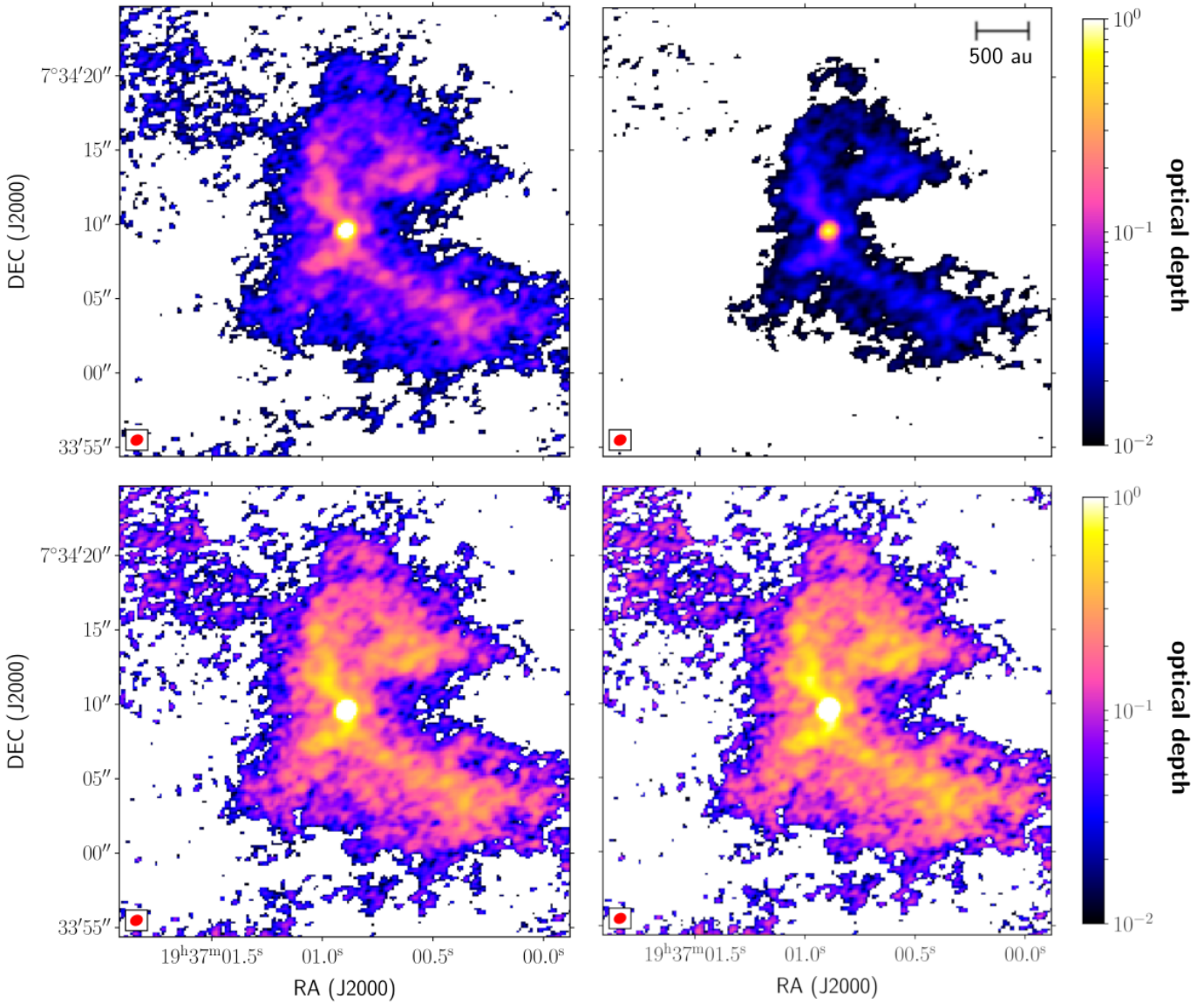


Fig. C.1: Expected optical depth maps for the four molecular tracers (see text in Section C for details). *Top left:* C^{17}O (J=1-0). *Top right:* DCO^+ (J=3-2). *Bottom left:* H^{13}CO^+ (J=1-0). *Bottom right:* H^{13}CO^+ (J=3-2).